Regional and Seasonal Trends in Tropical Ozone from SHADOZ Profiles: Reference for Models and Satellite Products

9 October 2021

Anne M. Thompson[1,2*], Ryan M. Stauffer[1], Krzysztof Wargan[1,3] , Jacquelyn C. Witte[4], Debra E. Kollonige[1,3], Jerald R. Ziemke[1,4]

[1]NASA/Goddard Space Flight Center (GSFC), Greenbelt, MD, USA anne.m.thompson@nasa.gov; ORCID: 0000-0002-7829-0920; ryan.m.stauffer@nasa.gov; ORCID: 0000-0002-8583-7795

[2]Joint Center for Earth Systems Technology (JCET)/University of Maryland-Baltimore County, Baltimore, MD

[3]Science Systems and Applications, Inc., Lanham, MD, krzysztof.wargan-1@nasa.gov; ORCID: 0000-0002-3795-2983; debra.e.kollonige@nasa.gov; ORCID: 0000-0002-6597-328X;

[4]National Center for Atmospheric Research Earth Observations Laboratory, Boulder, CO jwitte@ucar.edu; ORCID: 0000-0002-4110-5277

[5]Morgan State Univ., Baltimore, MD, jerald.r.ziemke@nasa.gov; ORCID: 0000-0002-5575-3654

*Corresponding author: Anne M. Thompson (anne.m.thompson@nasa.gov)

Key Points:

- Trends (1998-2019) in free troposphere (FT) O_3 at 5 SHADOZ sites are ~(1-4)%/decade, lower than some satellite or aircraft profile estimates
- Corresponding lowermost stratospheric (LMS) O_3 changes are ~(-3)%/decade, coinciding with an increase in tropopause height
- Both FT and LMS O_3 trends vary seasonally and regionally, defining new references for evaluating assessment models and satellite products

Keywords: Tropical Tropopause, Ozone Trends, Lower Stratosphere, Free Troposphere, SHADOZ

Index Terms: 341, 365, 1620, 3309, 3314

Abstract. Understanding lowermost stratosphere (LMS) ozone variability is an important topic in the trends and climate assessment communities because of feedbacks among changing temperature, dynamics and ozone. LMS evaluations are usually based on satellite observations. Free tropospheric (FT) ozone assessments typically rely on profiles from commercial aircraft. Ozonesonde measurements constitute an independent dataset encompassing both LMS and FT. We used Southern Hemisphere Additional Ozonesondes (SHADOZ) data (5.8°N to 14°S) from 1998-2019 in the Goddard Multiple Linear Regression model to analyze monthly mean FT and LMS ozone changes across five well-distributed tropical sites. Our findings: (1) both FT (5-15 km) and LMS (15-20 km) ozone trends show marked seasonal variability. (2) All stations exhibit FT ozone increases in February-May (up to 15%/decade) when the frequency of convectively-driven waves have changed. (3) After May, monthly ozone changes are both positive and negative, leading to mean trends of +(1-4)%/decade, depending on station. (4) LMS ozone losses reach (4-9)%/decade mid-year, correlating with an increase in TH as derived from SHADOZ radiosonde data. (5) When the upper FT and LMS are defined by tropopause-relative coordinates, the LMS ozone trends all become insignificant. Thus, the 20-year decline in tropical LMS ozone reported in recent satellite-based studies likely signifies a perturbed tropopause rather than chemical depletion. The SHADOZ-derived ozone changes highlight regional and seasonal variability across the tropics and define a new reference for evaluating changes derived from models and satellite products over the 1998 to 2019 period.

Plain Language Summary. Understanding free troposphere (FT) and lowermost stratosphere (LMS) ozone trends is important. If FT ozone increases, it will augment global warming. If LMS ozone has declined in the past 20 years it could mean that something is amiss in atmospheric conditions despite successes of the Montreal Protocol to eliminate ozone-depleting chemicals from the stratosphere. This study used high-accuracy, high-resolution (~150 m) ozone profiles from balloon-borne sondes to determine changes over the tropics. The data come from five sites in the Southern Hemisphere Additional Ozonesondes (SHADOZ) archive covering 1998-2019. A summary of results: (1) both FT (5-15 km) and LMS (15-20 km) ozone trends show marked seasonal variability. (2) All stations exhibit strong positive FT ozone trends in the February-May period but annual means at several stations comparable to the IAGOS record are ≤2%/decade. (3) LMS ozone losses range from (4-9)%/decade mid-year and appear to be an artifact of an increasing tropopause height. Therefore, the 20-year decline in tropical LMS ozone published in satellite-based studies may signify a perturbed tropopause, i.e., a climate signal. Our SHADOZ-derived ozone trends are available for models, challenging them to reproduce the regional and seasonal variations we find in recent trends.

1 Introduction

1.1 Trends in Free Tropospheric and Lowermost Stratospheric Ozone

Trends in tropical free tropospheric (FT) ozone have been featured in studies that use model results (*Zhang et al.,* 2016), satellite data (*Gaudel et al.,* 2018; *Ziemke et al.,* 2019) and commercial aircraft profiles (*Gaudel et al.,* 2020). *Gaudel et al.* (2018) summarize global uncertainties, displaying trends in tropical tropospheric ozone from five satellite-derived maps

that disagree in magnitude and even sign. Changes based on various Aura/OMI (2005-2016) products ranged from ~(10-25)%/decade. Using commercial aircraft data (http://iagos.org; In-service Aircraft for a Global Observing System) from a small number of urban airports in the northern tropics, *Gaudel et al.* (2020) report trends in tropical FT ozone equivalent to +(3-5)%/decade.

Studies with satellite data, including Aura OMI and MLS, also reflect uncertainty in both FT and LMS ozone trends over the past 15-20 years. Recent work with merged satellite datasets (SWOOSH, GOZCARDS, Merged SBUV; *SPARC/IO3C/GAW*, 2019) in the mid to lower stratosphere, along with chemistry-transport models (*Stauffer et al.,* 2019) and ozone assimilations, indicate the uncertainty of possible LMS ozone trends (*Ball et al.,* 2018; *Chipperfield et al.,* 2018; *Wargan et al.,* 2018), at least on a zonally averaged basis. For example, the products summarized by *Ball et al.* (2018), suggest a 20-yr (1998-2016) lowermost stratospheric (LMS) ozone loss up to 3%/decade, whereas *Wargan et al.* (2018; their Figure 3) show a comparable *increase* in tropical LMS ozone over the same period. A new study (*Szelag et al.,* 2020) with four satellite products reports LMS ozone losses of (2-3)%/decade in the tropics, a value that agrees with the most recent analysis of satellite data and with many models (*Ball et al.,* 2020).

Ozonesonde data are widely used by the scientific community for satellite validation and model evaluation, especially in the region from ~5-20 km, where uncertainties in most satellite measurements are relatively large and feedbacks among temperature, dynamics, ozone and water vapor are complex and important. SHADOZ (Southern Hemisphere Additional Ozonesondes; *Thompson et al.,* 2003a; 2012) is a 14-station tropical and subtropical network that has archived > 9000 profiles since 1998. In this study we determine trends in tropical FT and LMS ozone trends with reprocessed v06 SHADOZ profiles (*Thompson et al.,* 2017; *Witte et al*., 2017; 2018) that are better resolved (100-150 m in the vertical) than satellite measurements below 20 km. Thus, with a single data set interannual and seasonal variability throughout the FT, LMS and the critical tropopause transition layer between them are analyzed. There are other advantages of SHADOZ data. The SHADOZ measurements, distributed across eight tropical stations (*Thompson et al.*, 2003a), capture geographical variability and cover troposphere and stratosphere with ~5% precision. Most SHADOZ locations are relatively free of urban influence so trends in FT ozone represent changes in background ozone over a large

segment of the tropics. Another advantage of the SHADOZ data is that potential temperature readings from the radiosondes accompanying the ozonesonde launches provide direct information on dynamical factors that may be related to oscillations and trends.

1.2 Role of Climate Oscillations and Convection in Tropical Ozone Variability

Early studies of FT and LMS ozone variability with SHADOZ profiles focused on convective influences (*Folkins et al.,* 2000; 2002) and biomass burning (*Oltmans et al.,* 2001) over the western Pacific. More generally, *Thompson et al.* (2003b) showed that a mixture of dynamical and chemical influences determines FT ozone seasonal patterns at all SHADOZ stations. This view has been confirmed in studies of field campaigns (*Swap et al.,* 2003; *Thouret et al.,* 2009) and satellite observations (*Nassar et al.,* 2009).

ENSO-perturbed patterns of convection, precipitation and fire lead to variability in FT and LMS ozone profiles that vary station to station. In some cases, the ENSO leads to positive ozone anomalies; at other locations, ozone may decrease (*Thompson and Hudson,* 1999; *Randel and Thompson,* 2011). *Thompson et al.* (2001) used sonde and satellite data to demonstrate that even when fires cause exceptional pollution, as over Indonesia in 1997-1998, dynamical anomalies like the ENSO and Indian Ocean Dipole are major factors in a tropospheric ozone buildup. Other studies linking dynamics and FT and LMS ozone variability have examined the QBO (*Witte et al.,* 2008). Compared to HALOE on UARS (Halogen Occultation Experiment, Upper Atmosphere Research Satellite), SHADOZ sonde profiles show more structure in the LMS. Employing different statistical approaches, *Lee et al.* (2010) and *Randel and Thompson* (2011) found that QBO and ENSO impacts on FT and LMS ozone varied among stations within ±12 degrees latitude of the equator over the first 12 years of SHADOZ (1998-2009).

Thompson et al. (2011) reported on convectively-generated wave activity in the LMS for ten stations over the first decade (1998-2007) of the SHADOZ record. Laminae in ozone and potential temperature profiles were used to identify vertical displacements in segments up to 20 km that are attributed to convectively-generated waves (*Grant et al*., 1998). Using a Gravity Wave Index (GWI) based on laminae frequency, ozone variations were linked to the ENSO cycle (*Thompson et al.,* 2011). Strong relationships between gravity waves and ozone vertical structure are also indicated when FT ozone profiles are classified by Self-Organizing Maps (SOM; *Jensen et al.,* 2012; *Stauffer et al.,* 2018). The lowest ozone mixing ratios from ~5 to 15 km at SHADOZ stations coincide with the most intense convective activity, as indicated by wind

velocity potential, geopotential height, cloud cover, etc. Profiles with the highest ozone mixing ratios occur under stable meteorological conditions along with elevated concentrations of pollutants as seen by satellite. Signatures of the Madden-Julian Oscillation in ozone variations over the western Pacific/eastern Indian Ocean have been reported in SHADOZ profiles (*Stauffer et al.,* 2018) and in satellite estimations of tropospheric ozone (*Ziemke and Chandra,* 2003).

1.3 This Study

The uncertainty in lower atmospheric ozone changes over the past two decades and the documented impact of seasonal convection and climate oscillations on tropical ozone are motivation for examining ozone variability and trends with the 22-year SHADOZ record. First, we review seasonal and regional variations in FT and LMS ozone SHADOZ observations and convective activity as signified by ozone and radiosonde laminae. Second, trends in ozone profiles from 1998-2019 are determined with a standard Multiple Linear Regression (MLR) model. To investigate possible mechanisms for FT and LMS ozone changes, the MLR model is also applied to tropopause height derived from the SHADOZ radiosondes. We address the following questions:

- What are the trends, if any, in FT and LMS ozone in the tropics?
- Are there regional and/or seasonal variations in the trends?
- Do the sonde data provide useful information on dynamical factors connected to trends?

Depending on the station location we find negligible to small trends in ozone with distinct seasonality over the 22-year period, positive in the FT and negative in the LMS. The FT changes are strongest in February to May, when ozone is a minimum, and become negative about half the time during the remainder of the year. The LMS trend maximizes mid-year when there is an increasing trend in tropopause height (TH). The monthly averaged ozone and TH data along with the corresponding MLR model best-fit output are available to the satellite and modeling communities as an objective reference for their products. Data and analysis methods appear in **Section 2** with Results and Discussion in **Section 3. Section 4** is a summary.

2. Data and Methods of Analysis

2.1 FT and LMS Definitions

The analyses below span the surface to 20 km with the main results discussed referring to two FT segments: 5-10 km; 10-15 km. Ozone and pressure-temperature-humidity (P-T-U) data

below 5 km are not used because sampling times vary among stations. Station launch times are subject to change; at one SHADOZ station, for example, a trend in boundary-layer ozone was reported that was an artifact of a 5-hr launch change (*Clain et al.,* 2009; *Thompson et al.,* 2014). We use 15-20 km for the LMS, because this is where convective impacts on waves maximize (*Thompson et al.,* 2011) and where *Randel et al.* (2007) identified a distinct ozone annual cycle driven by the Brewer-Dobson circulation. The LMS includes most of the tropical tropopause layer (13.5-18.5 km) and several km above the tropical cold-point and thermal lapse-rate tropopauses over the SHADOZ sites (*Selkirk et al.,* 2010; *Thompson et al.,* 2012).

2.2 Reprocessed SHADOZ Data

Ozone data are taken from the SHADOZ archive (https://tropo.gsfc.nasa.gov/shadoz); the profiles measured originate from electrochemical concentration cell ozonesondes coupled to standard radiosondes. For analysis of tropical ozone for the years 1998-2019, we use v06 data from eight of the 14 long-term stations (**Table 1**) that are located between 5.8N and 14S. For more reliable statistics three of the "stations" or "sites" as they are referred to (**Figure 1**), are based on combining profiles from pairs of launch locations abbreviated as follows: SC-Para for San Cristóbal-Paramaribo; Nat-Asc for Natal-Ascension; KL-Java for Kuala Lumpur-Watukosek. For each station pair in **Figures S1-S3** (left panels) the time-series of the ozone column amounts (in Dobson Units, 1 DU = 2.69 x 10^{16} cm^{-2}) at three altitude ranges appear. The ozone column amounts in the lower FT (5-10 km), range from 5-15 DU for SC-Para (**Figure S1a**) but extend from 5 to 20 DU for Nat-Asc (**Figure S2a**). In the eastern Indian Ocean, over KL-Java, (**Figure S3a**), the ozone columns in the lower FT range from 5-10 DU. In the upper FT (10-15 km) the typical lower limit for column ozone is 3 DU at all three sites (**Figures S1b, S2b, S3b**) but the means show distinct differences: 6 DU at SC-Para; 8.5 DU for Nat-Asc; and < 5 DU at KL-Java. The right-side panels for each pair in **Figures S1-S3**, that display the mean monthly ozone column amount ($\pm$1 σ), further clarify the pairing choices. *Jensen et al.* (2012) established close similarities of Natal and Ascension FT ozone from 12 years of SHADOZ soundings along with related meteorological factors using self-organizing maps (Section 2.5). Note in **Figure S2e** the close agreement of upper FT column ozone at the two stations, especially from August to December when there is a broad seasonal maximum. Although column ozone amounts at Paramaribo (**Figure S1e**) resemble those of Natal and Ascension in the upper FT (**Figure S2e**), Paramaribo has a 30-40% smaller ozone column than Natal and Ascension in the lower FT (cf

Figures S1d and **S2d**). In the LMS there is a steady dropoff in SC-Para ozone from September to December (**Figure S1f**) 16 to 12 DU, that does not occur over Natal and Ascension (cf **Figure S2f**). Thus, although Natal is approximately the same distance from Paramaribo and Ascension, the similarities in seasonal ozone patterns argue for pairing Natal with Ascension instead of Paramaribo.

A second approach to pair selection is based on comparing satellite estimates for tropospheric ozone to total tropospheric ozone measured by the sondes. In the upper panel of the frames in **Figure S4** the OMI/MLS estimate of monthly-averaged tropospheric column ozone $TrCO_{sat}$ (*Ziemke et al.,* 2006; *Ziemke et al.,* 2019; 1^{o}x1.25^{o} product, co-located at the 8 tropical SHADOZ sites) is presented with the monthly mean integrated tropospheric column ozone from the sondes, $TrCO_{sonde}$. The lower panels in **Figure S4** display the mean offsets of the two TrCO quantities in DU and %, along with the average offset. A scatterplot of all TrCO comparisons for the 8 stations (**Figure S5a**) gives a $r^2 = 0.72$; there is markedly less correlation when $TrCO_{sat}$ and $TrCO_{sonde}$ for the four subtropical SHADOZ stations are analyzed (**Figure S5b**). Regional differences in the offset (sonde-satellite in %) support the pairings in **Figures S1-S3**. For example, $TrCO_{sat}$ ranges from 6-12% low in the eastern Indian Ocean and Atlantic regions but is 3% higher than $TrCO_{sonde}$ at Samoa; for Fiji (not shown), $TrCO_{sat}$ exceeds $TrCO_{sonde}$ by 6%.

The v06 SHADOZ data, reprocessed in 2016-2018, reduced inhomogeneities due to instrument or data-handling changes (*Witte et al.,* 2017; 2018) such that sonde total ozone column (TOC) amounts agree with ground-based or satellite data within 2% for all but one station. Data from a number of SHADOZ stations display a 3-6% dropoff in TOC after 2013 (*Sterling et al.,* 2018; *Stauffer et al.,* 2020) relative to satellite and/or ground-based readings. For the Costa Rican station (10N, 84W), a ~5% dropoff occurs in FT ozone (*Stauffer et al.,* 2020) so those measurements are not used. For the stations analyzed here, the dropoff is confined to readings above 50 hPa (~20 km) and does not affect the results.

2.3 Multiple Linear Regression Model (MLR)

In order to quantify factors leading to seasonal and interannual variability as well as trends, a standard MLR model (original version *Stolarski et al.,* 1991, updated in *Ziemke et al.,* 2019) is applied to monthly mean ozone profiles for the 5 stations: the 3 combined sites, Nairobi and Samoa. The reasoning behind the choice of station combinations was summarized in **Section 2.2** and **Figures S1-S3**. In order to account for any biases that could arise from intersite ozone

differences between the chosen pairs, we calculate ozone anomalies from the individual station's monthly climatology for all profiles before combining the pairs into monthly means and computing the MLR ozone trends. This procedure avoids "false" trends resulting from periods where the data record shifts to being available at only one of two stations (e.g. 2014-2019 at KL-Java; **Figure S3**). This same technique is applied to the 380 K potential temperature surface (tropopause height) as discussed below. For consistency, the ozone and tropopause height anomaly calculations are also applied to individual stations, where comparisons of MLR ozone and tropopause height trends without calculating anomalies show negligible differences.

The MLR model includes terms for annual and semi-annual cycles and oscillations prevalent in the tropics: QBO, MEI (Multivariate ENSO Index, v2) and IOD DMI (Indian Ocean Dipole Moment Index; only for KL-Java):

$$O_3(t) = A(t) + B(t) + C(t)MEI(t) + D(t)QBO1(t) + E(t)QBO2(t) + F(t)IOD(t) + \varepsilon(t)$$

where t is month. The coefficients are as follows: A through F include a constant and periodic components with 12, 6, 4, and 3 month cycles, where A represents the mean monthly seasonal cycle and B represents the month-dependent linear trend. The model includes data from the MEIv2 (https://www.esrl.noaa.gov/psd/enso/mei/), the two leading QBO EOFs from Singapore monthly mean zonal radiosonde winds at 10, 15, 20, 30, 40, 50, and 70 hPa levels, and IOD DMI (https://psl.noaa.gov/gcos_wgsp/Timeseries/Data/dmi.had.long.data). The ε(t) is the residual, i.e., the difference between the best-fit model and the raw data. Monthly ozone data and model fits for the mid FT (5-10 km) and LMS (**Figures S6 and S7**) are well-correlated; for the LMS, for example, the correlation coefficients are r = 0.83-0.90 (**Figure S7**). The IOD DMI term is included for KL-Java because that was the only station where the IOD DMI accounted for an ozone response different from zero with a p-value < 0.05. The 95% confidence intervals and p-values for each term in the MLR model and presented in this study are determined using a moving-block bootstrap technique (10,000 resamples) in order to account for auto-correlation in the ozone time series (*Wilks,* 1997). Recent ozone trends studies (*Chang et al.,* 2020; *Cooper et al.,* 2020) have discouraged the practice of distinguishing levels of statistical significance. Therefore, while we focus on ozone trends that are larger than the 95% confidence interval (p-value < 0.05), all trend values, 95% confidence intervals, and p-values are presented in the results section (**Section 3.2.1, Table 1**).

The MLR model was separately applied to the monthly mean ozone profile anomalies at 100 m resolution, and the monthly mean partial column ozone anomaly amounts from 5-10 km, 10-15 km, and 15-20 km. We also applied the MLR model to the monthly mean tropopause altitude anomaly at each station, defined as the 380 K potential temperature surface (e.g., *Wargan et al.*, 2018). It turns out that tropopause height (TH) and LMS ozone trends are strongly correlated. Thus, the MLR analysis was also performed for the ozone column amount anomalies referenced to the tropopause. In that case LMS ozone trends refer to changes in the 5 km above the tropopause with the FT extending from the tropopause to 10 km below the tropopause (**Section 3.3.2, Table 2**).

2.4 Laminar Identification (LID) and GW Indices

The Laminar Identification (LID) method was used to identify convective signatures in ozone profiles for the 1998-2009 SHADOZ data (*Thompson et al.,* 2011). The LID technique, applied here to the 1998-2019 record (**Table 1**), is based on the coherence of laminae in each ozone and potential temperature profile pair; laminae are identified as deviations from running means calculated every 0.5 km from surface to 20 km. When the potential temperature and ozone laminae at a given level are strongly correlated ($r > 0.7$), as often occurs in the LMS, the presence of a convectively-generated gravity wave (GW) is inferred. The GW occurrence is a proxy for a convective event. Convective influence is quantified by the monthly GW frequency (GWF), defined as the percent ratio of profiles exhibiting the GW signal relative to the total number of profiles within a given month.

2.5 Self-Organizing Maps (SOM)

We have used SOM, a machine-learning technique, to classify ozone profiles in terms of meteorological or chemical influences (*Stauffer et al.,* 2016). The entire set of ozone profiles for each station is ingested into the SOM code to obtain initial nodes (i.e., centroids or means for each cluster) via a linear interpolation between the two largest components of the ensemble. Subsequent iterations assign a given profile to its "best match" until a cluster mean is obtained. We adopt key elements of the procedure in *Stauffer et al.* (2018): 1) a four-cluster 2x2 SOM is used to avoid clusters with too few members for meaningful statistics (cf *Jensen et al.,* 2012); 2) SOM clusters are numbered 1 to 4 based on the cluster "mean" ozone profile. The result is a consistent definition of Cluster 1 and Cluster 4 as "low" and "high" ozone for each site, respectively. Links among SOM ozone profile shape, GWF, and trends are investigated.

294

295 ## 3 Results and Discussion

296 ### 3.1 Seasonal Cycles in Ozone and Convective Influence

297 **Figure 2** displays the 5-site monthly ozone climatology from the surface to 20 km. Regional
298 differences in vertical structure within the FT are pronounced. For example, the contours
299 representing the 60-90 ppbv range never appear in middle FT ozone over KL-Java or Samoa
300 (**Figures 2d,e**). Conversely, FT ozone values ≤ 30 ppbv (light yellows) in the middle FT never
301 appear over the equatorial Americas (SC-Para, **Figure 2a**), Nat-Asc or Nairobi (**Figures 2b,c**).
302 These contrasts partly reflect regional differences in ascending vs. descending nodes of the
303 Walker circulation. The mean TOC over the south tropical Atlantic Ocean is 5% greater than
304 over the western Pacific, giving rise to the well-known tropospheric zonal wave-one (*Thompson*
305 *et al.,* 2003b). Compared to the FT, there is less regional variability in LMS ozone (Figure 8 in
306 *Thompson et al.*, 2017). At all the stations, above ~16 km, the colors and contours are similar:
307 nearly uniform over the year with mixing ratio contours of 100 ppbv and 200 ppbv similarly
308 spaced.

309 A large seasonal signal in LMS ozone is associated with the Brewer-Dobson circulation
310 (**Figure 3a**; cf *Randel et al.,* 2007). FT ozone seasonality (**Figures 3b,c**) is less uniform due to the
311 timing of various dynamical and chemical influences across sites. However, the minima for all
312 sites occur in January through April or May except for a second short minimum after July over
313 KL-Java. Localized FT ozone maxima occur largely from imported fire pollution: SC-Para in
314 March and after July (**Figure 2a**); features at 6-8 km over Nat-Asc, Samoa and KL-Java
315 September to November (**Figures 2b-d**); Nairobi (**Figure 2c**) in June and after August. Month-
316 to-month anomalies from annual mean FT ozone (**Figure 3b,c)** in the 5-10 km and 10-15 km
317 layers appear complex for all stations. The vertical dashed lines appearing on **Figures 2, 4, and**
318 **5** mark when ozone anomalies from the annual mean over 5-15 km change sign, indicating
319 transitions in seasonal ozone amount and convective activity. These transitions in ozone
320 anomalies display some regional similarities, e.g., the SC-Para and Nat-Asc pairs (**Figures 4a** and
321 **4b**). Nairobi and KL-Java (**Figures 4c** and **4d**), at opposite ends of the Indian Ocean, both exhibit
322 shifts in March and December. Convective influence, given by GWF (**Figure 5**), with transitions
323 marked as for ozone, shifts during the same periods. GWF reaches 50-60% during January to
324 April at all locations (**Figure 5**), during which ozone minima above 8 km, attributed to

convective redistribution of near-surface lower ozone air (**Figure 2**), appear over all stations. Comparing **Figures 4 and 5** reveals the correspondence between increased (decreased) convective activity and decreased (increased) ozone amounts, especially in the upper FT and LMS.

3.2 FT Ozone Changes (1998-2019)

In **Figure 6** FT and LMS changes in ozone mixing ratio (%/decade during 1998-2019) are displayed, based on monthly mean trends computed with the MLR model. Corresponding values in three layers appear in **Table 1.** The percentage values in **Figure 6** and **Table 1** are the result of dividing the MLR B(t) term by the A(t) annual cycle of ozone term. The MLR-calculated A(t) annual cycle derived from monthly mean ozone profiles (i.e., no anomaly calculation) is used to convert the B(t) trend in ppmv/decade (profiles) or DU/decade (partial columns) to %/decade. Ozone trends for both percent/decade and DU/decade are given in **Tables 1 and S1**, respectively (see **Section 3.3.2** for Tables 2 and S2). Shades of red (blue) in **Figure 6** represent ozone increases (decreases); cyan hatching denotes trends with p-values < 0.05. The annual mean trends in **Table 1** are computed by taking the average of the 12 monthly trends in DU, and dividing by the mean seasonal ozone in DU to yield the annual percentage trend. **Table T1** presents the trends of Table 1 in DU/decade for the same layers.

3.2.1 FT Ozone Trends: Regional and Seasonal Variability

For all five stations in **Figure 6**, there is a pattern of strong ozone increase at various altitudes in the FT in February to April or May. In terms of column-integrated ozone amounts for individual stations, these changes range from 0 to +16%/decade (except for SC-Para in February), as displayed in **Table 1**. However, on an annually averaged basis ozone trends are only +(1-2)%/decade and +(0-4)%/decade in the 5-10 km and 10-15 km layers, respectively. Indeed, except for the robust +3.9%/decade over Nat-Asc in the 10-15 km layer, FT ozone increases at the other stations average <2%/decade (**Table 1**).

Figure 7, that presents monthly mean ozone column changes in the two FT layers, illustrates regional and seasonal variability. For example, the dominant impact of southern African and South American fires on Nat-Asc and Samoa FT ozone in July through November is well-documented (*Oltmans et al*., 2001; *Thompson et al.,* 2003b). A near-absence of trends over these sites (**Table 1**) from July (Samoa) and August (Nat-Asc) through November (**Figures 6b,e)** signifies little change in fires since 1998, consistent with a lack of trends in pyrogenic NO_x over

356 the past 25 years reported in *Gaudel et al.* (2020; their Figure 5). There is also an increase in 5-
357 10 km ozone over KL-Java (**Table 1**) in the August to October period, (1.8-3.9)%/decade, which
358 is the typical fire season in Indonesia (*Pan et al.,* 2018). The much stronger FT ozone increases
359 over KL-Java (**Figure 6d**) in February-April, (2.8-15.7)%/decade (**Table 1**), may be related to
360 the southeast Asian fire season (*Liao et al.,* 2021) and/or to growing urban emissions (*Zhang et*
361 *al.,* 2016; *Gaudel et al.*, 2020; *Cooper et al.,* 2020).

362 How do the FT ozone trends based on SHADOZ profiles compare to other analyses? *Zhang et*
363 *al.* (2016) and *Gaudel et al.* (2018) reported on tropospheric ozone changes at different periods
364 within 1994-2015. In both those studies, satellite-derived tropospheric ozone columns and
365 IAGOS commercial aircraft profiles include ozone below 5 km so the results are not directly
366 comparable to the FT SHADOZ-based trends. However, *Gaudel et al.* (2018; Figures 4 and 24)
367 also presented analysis based on the trajectory-mapped ozonesonde climatology of *Liu et al.*
368 (2013). Those tropical trends, that included SHADOZ profiles, displayed more regionally varying
369 trends than most satellite products.

370 In the more recent *Gaudel et al.* (2020) study, where their IAGOS "Malaysia" data include
371 landing/takeoff profiles at Jakarta, Indonesia, the FT ozone changes over the period 1995 to
372 2016 are ~+5%/decade. This is about twice the annually averaged increase computed from the
373 SHADOZ KL-Java 5-10 km ozone trends from 1998-2019 (**Table 1**). However, **Figure 7** shows
374 that the KL-Java trends are the most seasonally variable of the 5 stations analyzed. In February
375 through April, the KL-Java trends are +(13-16)%/decade ($p<0.05$), falling to mostly negative
376 values, -(2-8)%/decade, in the 5-10 km and 10-15 km layers, the remainder of the year. In
377 *Gaudel et al.* (2020) the northern tropics is represented by IAGOS profiles over northern South
378 America; the IAGOS Cayenne, French Guiana, landings/takeoffs are not far from Paramaribo. The
379 Cayenne IAGOS trends show a FT ozone increase ~3%/decade. The SHADOZ-based trends at SC-
380 Para on average are +2%/decade (**Table 1**). However, as for KL-Java, there is considerable
381 seasonal divergence. In February-April at SC-Para, the FT ozone increase ranges from +(1 to
382 12)%/decade, and +(3 to 7)%/decade August to November (**Figure 7**). In January, June and
383 December, the SC-Para trend is actually slightly negative.

384 A noteworthy point of agreement between the IAGOS and SHADOZ-based records is that in
385 both cases, the largest positive trends (**Tabel 1, Figure 7**) occur at the lowest-ozone season
386 (January to April, **Figures 3b,c**), i.e., the minimum ozone amounts have increased over the past

several decades. In general, the SHADOZ and IAGOS data provide complementary information on trends. With SHADOZ stations, except for KL-Java, at more remote locations than most IAGOS cities, the SHADOZ results better represent changes in background ozone. The distinctive seasonality of the SHADOZ trends indicates dynamical changes that probably underlie chemical influences that are known to be changing in the tropics (*Gaudel et al.,* 2018; 2020). The next section examines one aspect of possible dynamical influences on the SHADOZ ozone trends.

3.2.2 Role of Convection in FT Ozone Changes

Sections 3.1 and **3.2.1** described an implicit role for convection in the seasonal variability of FT ozone. The annual cycles of FT ozone provide context for the changes shown in **Figure 6.** The most robust positive FT ozone trends, predominantly from February to May (**Table 1, Figure 7**) take place when FT ozone is at its annual minimum (**Figures 3b,c**) and convective activity is high as signified by GWF (**Figure 5**). This can be seen seen when the relationship between ozone profile variability and convection are examined using the LID and SOM methods (**Sections 2.4** and **2.5**). The classification of ozone profiles for several SHADOZ sites in a 2x2 SOM (*Stauffer et al.,* 2018) established an anticorrelation between FT ozone mixing ratios and convective activity, where the latter was quantified by meteorological parameters at sonde launch time (Figure 7 in *Stauffer et al.,* 2018). The SOM in **Figure 8**, based on the 5-station data analyzed here, shows similar relationships. Clusters displaying the lowest (Cluster 1) and highest (Cluster 4) profiles of ozone are illustrated. The characteristic S-shapes of upper FT ozone profiles in Cluster 1 (**Figure 8a)** display the lowest mixing ratios whereas much of the elevated ozone in Cluster 4 (**Figure 8b)** derives from imported pollution at 5-10 km. The GWF corresponding to Cluster 1 (**Figure 8c)**, representing maximum convection, is dominated by January-May profiles (**Figure 8e**), that is, when there are positive FT ozone changes at all sites. Cluster 4 ozone mixing ratios throughout the FT and LMS (**Figure 8b**) are much greater than Cluster 1 (**Figure 8a**) and correspond to the season when the stations are most affected by transported pollution from biomass fires (**Figure 8f**). The fire season impacts are strongest from June through November except for KL-Java where a March through May maximum corresponds to the southeast Asia burning season (the seasonality can be modified under conditions of a major ENSO; *Thompson et al.,* 2001; *Field et al.,* 2016; *Pan et al.,* 2018). **Figure 8d** shows that for all stations, convection as indicated by GWF is reduced for the highest-ozone profiles that mostly occur during the burning season: April-May for KL-Java; after July for the

418 other 4 sites (**Figure 8f**). GWF in Cluster 4 (**Figure 8d**) remains above 50% for KL-Java with
419 April and October the most prevalent months (**Figure 8f**); the latter coincides with the late
420 Asian monsoon period. However, for Cluster 4 the maximum GWF is 47% at Nairobi, compared
421 to 64% for Cluster 1 (**Figure 8e**). For SC-Para, Na-Asc and Samoa the maximum GWF drops
422 below 30% (**Figure 8d**).

423 The connection of the ozone trends to convection using the GWF proxy is not clear, but there
424 are correlations among GWF changes and ozone trends. For example, computing the difference
425 in GWF for the first five years (1998-2002) and the latest five years (2015-2019) in the SHADOZ
426 record (**Figure 9**) shows correspondence between an increasing GWF trend and decreasing LMS
427 ozone, and decreasing GWF and increasing FT ozone. At all sites the GWF declines between
428 January and June (**Figure 5**), albeit weakly at Samoa (**Figure 9e**) when segments of FT ozone
429 are increasing (**Figures 6** and **7**)**.** If there is less convection over a station, signifying less vertical
430 mixing and detrainment, FT ozone would accumulate. Mid-year, particularly over KL-Java
431 (**Figure 9d**), GWF increases and there is a corresponding upper FT negative ozone trend
432 (**Figure 6d**). Whether or not mid-year changes in GWF (**Figure 9**), presumably signifying
433 increases in convection, play a role in LMS ozone and TH trends (**Section 3.3.1** below) is
434 unclear. The interaction among changes in convection and trends in ozone and TH (**Section**
435 **3.3.2**) cannot be determined from the SHADOZ profiles alone. Independent data, e.g., OLR,
436 dynamical parameters from re-analyses and model simulations, need to be examined.
437
438 **3.3 LMS Ozone Trends**
439 **3.3.1 LMS Ozone and TH Trends: Seasonal Variability**
440 As for the FT ozone trends, Figure 6 shows distinctive seasonality in LMS ozone trends
441 with layers of 5%/decade losses for 1998-2019 after May at all five stations. At KL-Java (**Figure**
442 **6d**) ozone losses are greater, with layers of depletion at 15-20%/decade after August. The
443 corresponding LMS column ozone loss, annually averaged, is -5.8%/decade **(Table 1**), almost
444 twice the mean rate over SC-Para (**Figure 6a**): -3.1%/decade **(Table 1**). KL-Java is unique in
445 displaying a layer of ozone loss at 18-19 km in January (**Figure 6d**). However, there is also a
446 zone of increasing ozone in the LMS over KL-Java March-May between 15 and 18 km. A similar
447 feature, a positive ozone trend at 15-18 km in February-April, also appears over Nairobi (**Figure**

448 **6c**). For the Atlantic (Nat-Asc) to Nairobi (**Figures 6b,c**) the most substantial negative trends
449 are found in June through September.

450 The corresponding ozone column changes from 1998 to 2019 appear in **Table 1**, where p
451 values <0.05, signified by underlined, bold type, are the most significant. Although isolated
452 months display large LMS ozone losses (to -10%/decade), on an annually averaged basis, only
453 two stations, KL-Java (-[5.8± 2.8]%/decade) and SC-Para (-[3.1± 2.8]%/decade), have significant
454 negative trends. At Samoa (-[2.8± 3.4]%/decade) LMS changes are marginal. There is no LMS
455 ozone loss, on average, over Nat-Asc and Nairobi (**Table 1**). How do these values compare to the
456 updated satellite-based and model trends reported recently by *Ball et al.* (2020) who display
457 only zonal averages with no reference to regional variability? Given that the SHADOZ-based
458 LMS trends are positive over large regions and negative over others, the zonally averaged
459 negative trends (*Ball et al.,* 2020) may be overestimating tropical LMS ozone losses.

460 The first study of seasonality in lower stratospheric ozone trends – results reported as zonal
461 means for four merged satellite products – was published by *Szelag et al.* (2020). For all four
462 products, the season with the most negative trend is March-April-May, not after June as for the
463 SHADOZ stations in **Figure 6** and **Table 1.** However, the *Szelag et al.* (2020; Figure 4)
464 calculations may not be directly comparable to our analyses.

465 In contrast to the highly varied seasonal patterns of FT ozone (**Figures 3b,c**), the annual cycle
466 of LMS ozone (**Figure 3a**) is fairly uniform (*Randel et al.,* 2007). A comparison with the LMS
467 trends in **Figure 6** shows that (1) both positive and negative ozone changes occur during the
468 low-ozone time of year (January to May); (2) more negative, sustained LMS ozone trends take
469 place during the maximum-ozone period (June/July through October/November; **Figure 3a**).
470 This means that over the year, the magnitude of the annual LMS seasonal cycle has declined
471 slightly, i.e., the annual cycle is flattening.

472 **Figure 10** illustrates the trends in monthly LMS ozone (**Figure 10a**, %/decade) and TH
473 (**Figure 10b**, trend in the altitude of 380 K potential temperature [θ] surface in m/decade) as
474 computed from the MLR model for the five SHADOZ stations. After June, when the ozone loss is
475 most pronounced for all stations except Samoa, there is an increase in TH (**Figure 10b**) that is
476 correlated with the LMS ozone decrease. **Figure 3** shows that the annual LMS ozone cycle at
477 Samoa (14S latitude) differs from the more equatorial stations (5.8N-7.6S). The seasonal
478 patterns of the Samoa LMS ozone and TH trends (gray dashed in **Figure 10**) also diverges from

479 the other stations. There are two period of LMS ozone loss at Samoa (**Figure 10a**) with the
480 larger one taking place in April and May. These months of largest ozone loss coincide with the
481 greatest TH increase at Samoa, although the latter is only 50 m/decade, compared to the 100-
482 150 m/decade increase for the other for stations (**Figure 10b**).

483 ### 3.3.2 Dynamic Influences in LMS Ozone and Tropopause Height Trends

484 Because the LMS definition here is 15-20 km, it is reasonable to ask if the increased
485 tropopause height (a stratospheric [tropospheric] thickness reduced [increased] by 50-150 m)
486 is responsible for the negative LMS ozone trend over 1998 to 2019. To examine this possibility,
487 all ozone profiles were placed in coordinates relative to the 380 K potential temperature surface
488 (TH) prior to calculating monthly means and MLR trends (**Section 2.3**). Results are presented
489 for layers from 10 to 5 km below the TH, 5 km below the TH to the TH, and the TH to 5 km above
490 the TH (**Table 2**). Within the 5 km layer above the TH, as displayed in **Figure 11**, the monthly
491 trends have disappeared for all stations except for small LMS ozone increases at Nat-Asc and
492 Nairobi in the early part of the year, September-December at Nairobi and losses at Samoa in
493 June and July. However, **Table 2** does not show significant monthly or mean annual trends in
494 LMS ozone (p value <0.05) for any of the SHADOZ stations.

495 In summary, the annually averaged LMS ozone losses calculated with a fixed-altitude column
496 disappear when the ozone column is determined with a tropopause-defined LMS (**Table 2**). A
497 perturbed TH, possibly due to a changing climate, is associated with tropical LMS ozone losses
498 from June to November for four stations. The fact that LMS ozone might be increasing over two
499 stations at other times of year underscores the finding that TH influences, and perhaps other
500 dynamical impacts, are not regionally and seasonally uniform. A decisive role for dynamical
501 influences also suggests that where LMS ozone in the tropics is declining (*Ball et al.* 2018; 2020),
502 the cause is not because of chemical reactions.
503

504 ## 4 Summary

505 The 22-year SHADOZ record (1998-2019) of ozone profiles from five well-distributed tropical
506 regions has been used to compute trends in the FT (5-15 km) and LMS (15-20 km). Both FT and
507 LMS ozone trends exhibit pronounced regional and seasonal variability. We enumerate the
508 major results:

(1) There are robust FT ozone increases at all 5 SHADOZ stations, in thin layers from ~(5-25)%/decade, between February and May. The corresponding FT ozone column amounts typically average +(3-10)%/decade during that time; KL-Java is higher. However, both magnitude and direction of these trends vary considerably after May, with individual layers at all stations in the remaining months roughly half positive and half negative. The result is mean trends of +(1-4)%/decade, depending on the station.

(2) Due to a mismatch in sampling characteristics and time periods investigated, it is difficult to compare SHADOZ trends with those derived from satellite products or aircraft profiles. However, like the IAGOS-based study of *Gaudel et al.* (2020) that presented trends from several equatorial locations in South America and southeast Asia, the large SHADOZ FT trends from February to May indicate a shift to higher minimum ozone values. Four of the five SHADOZ stations are very remote and thus represent changes in background ozone. Their nuanced variations in seasonal and regional changes probably signify dynamical changes. As an example, we showed that the FT ozone trends in the early part of the year may be related to reduced convection as indicated by a change in wave activity (GWF).

(3) LMS ozone losses mostly take place later in the second half of the year when GWF (convective influence) and tropopause altitude both exhibit increases. The LMS trends are strongest in July to September, reaching –(4-9)%/year (ozone) and +150 m/decade (TH) at individual stations. Because the LMS ozone loss maximizes at the annual ozone maximum without a comparable increase at other times of year, the ozone cycle associated with the Brewer-Dobson Circulation has been flattening. The TH increase during the annual TH minimum indicates that the annual tropopause cycle is also diminished.

(4) When the LMS ozone trends are recomputed using ozone column segments referenced to the changing TH, the ozone losses disappear, even becoming slightly positive at two stations certain months of the year. This finding supports previous analyses that suggest LMS ozone losses since 1998 are dynamically, not chemically, driven.

Randel et al. (2007) and *Stolarski et al.* (2014) used satellite observations and meteorological analyses to describe multiple dynamical influences on LMS ozone. Our simplified study interprets FT and LMS ozone changes with reference to TH and a proxy for vertical motion that is inferred only from the sounding data. Model diagnostics are required to assess the roles of

changing chemistry in the troposphere and to evaluate the contributions of perturbed dynamics to FT and LMS ozone changes. Nonetheless, the relatively small, geographically distinct changes derived from SHADOZ profiles provide a reference for evaluating (1) LMS ozone trends derived from satellite products that do not include regional variability (*Ball et al.,* 2020; *Szelag et al.,* 2020) and (2) aircraft-based (*Gaudel et al.,* 2020) FT ozone trends. The relatively small SHADOZ trends show that large regions of the tropics do not exhibit year-round FT ozone increases, suggesting that increases in tropospheric ozone in the tropics are partly dynamical in origin and not solely a consequence of growing anthropogenic emissions.

We conclude that using the SHADOZ results to evaluate the regional and seasonal variability of satellite-based products and related models is an impartial way to establish their reliability for ozone trends assessments and predictions of FT and LMS ozone changes in the near future. This first report of an increasing tropopause height over SHADOZ sites is also a reference for satellite observations and models.

Acknowledgments

Support is gratefully acknowledged from the NASA Upper Air Research Program (K. W. Jucks, Program Manager), S-NPP and JPSS (J. F. Gleason, Project Scientist) and the NASA Post-doctoral Program to RMS. We are grateful to O. R. Cooper (CIRES/NOAA-CSL) and W. Randel (NCAR) for helpful comments. SHADOZ v06 profile data are available at https://tropo.gsfc.nasa.gov/shadoz/Archive.html. OMI/MLS data are available at https://acd-ext.gsfc.nasa.gov/Data_services/cloud_slice/new_data.html.

References

Ball, W. T., Alsing, J., Mortlock, D. J., Staehelin, J., Haigh, J. D., Peter, T., et al. (2018). Continuous decline in lower stratospheric ozone off sets ozone layer recovery, *Atmos. Chem. Phys.*, 18, 1379–1394, https://doi.org/10.5194/acp-18-1379-2018

Ball, W. T., Chiodo, G., Abalos, M., Alsing, J., Stenke, A. (2020) Inconsistencies between chemistry-climate models and observed lower stratospheric ozone trends since 1998, *Atmos. Chem. Phys*., 20, 9737–9752. https://doi.org/10.5194/acp-20-9737-2020

Chang, K.-L., Cooper, O. R., Gaudel, A., Petropavlovskikh, I., Thouret, V., (2020), Statistical regularization for trend detection: An integrated approach for detecting long-term trends from sparse tropospheric ozone profiles, *Atmos. Chem. Phys.,* 20, 9915-9938, https://doi.org/10.5194/acp-20-9915-2020

Chipperfield, M. P., Dhomse, S., Hossaini, R., Feng, W., Santee, M. L., Weber, M., et al. (2018). On the cause of recent variations in lower stratospheric ozone, *Geophys. Res. Lett*., 45, https://doi.org/10.1029/2018GL078071

Cooper, O. R., Schultz, M. G., Schröder, S., Chang, K-L., Gaudel, A., Benite, G. C., et al. 2020. Multi-decadal surface ozone trends at globally distributed remote locations. *Elem Sci Anth,* 8: 23. DOI: https://doi.org/10.1525/elementa.420

Field, R. D., van der Werf, G. R., Fanin, T., Fetzer, E. J., Fuller, R., Jethva, H., et al. (2016) Indonesian fire activity and smoke pollution in 2015 show persistent nonlinear sensitivity to El Niño-induced drought, *Proc. Natl. Acad. Sci. USA*. 2016 Aug 16; 113(33): 9204–9209. 10.1073/pnas.1524888113

Folkins, I., Oltmans, S. J., Thompson, A. M., (2000) Tropical convective outflow and near-surface equivalent potential temperatures, *Geophys. Res. Lett.,* 27, 2549-2552

Folkins, I. Braun, C., Thompson, A. M., Witte, J. C. (2002). Tropical ozone as in indicator of deep convective outflow, *J. Geophys. Res. Atmos.*, 107, D13, doi: 10.1029/2001JD001178

Gaudel, A., Cooper, O. R., Ancellet, G., Barret, B., Boynard, A., Burrows, J. P., et al. (2018). Tropospheric Ozone Assessment Report: Present-day distribution and trends of tropospheric ozone relevant to climate and global atmospheric chemistry model evaluation, *Elem. Sci. Anth*., 6: 39, doi: https://doi.org/10.1525/elementa.291

Gaudel, A., Cooper, O. R, Chang, K.-L., Bourgeois, I., Ziemke, J. R., Strode, S. A., Oman, L. D., et al. (2020). Aircraft observations since the 1990s reveal increases of tropospheric ozone at multiple locations across the Northern Hemisphere*, Science Advances,* 6, no. 34, eaba8272, doi: 10.1126/sciadv.aba8272

Grant, W. B., Pierce, R. B., Oltmans, S. J., Browell, E. V. (1998), Seasonal evolution of total and gravity wave induced laminae in ozonesonde data in the tropics and subtropics, *Geophys. Res. Lett.,* 25, 1863-1866, doi:10.1029/98GL01297

Jensen, A. A., Thompson, A. M., Schmidlin, F. J. (2012). Classification of Ascension Island and Natal ozonesondes using self-organizing maps, *J. Geophys. Res. Atmos.*, 117, D04302, doi10.1029/2011JD016573

Liao, Z., Ling, Z., Gao, M., Sun, J., Zhao, W., Ma, P., et al. (2021). Tropospheric ozone variability over Hong Kong based on recent 20 years (2000–2019) ozonesonde observation, *J. Geophys. Res. Atmos.*, 126, e2020JD033054, https://doi.org/10.1029/2020JD033054

Lee, S., Shelow, D. M., Thompson, A. M., Miller, S. K. (2010). QBO and ENSO variability in temperature and ozone from SHADOZ (1998-2005), *J. Geophys. Res. Atmos.,* 115, D18105, doi: 10.1029/2009JD013320

Liu, G., Liu, J., Tarasick, D. W., Fioletov, V. E., Jin, J. J., Moeini, O., et al. (2013) A global tropospheric ozone climatology from trajectory-mapped ozone soundings, Atmos. Chem. Phys., 13, 10659–10675, https://doi.org/10.5194/acp-13-10659-2013

Nassar, R., Logan, J. A., Megretskaia, I. A., Murray, L. T., Zhang, L., Jones, D. B. A. (2009) Analysis of tropical tropospheric ozone, carbon monoxide, and water vapor during the 2006 El Niño using TES observations and the GEOS-Chem model, *J. Geophys. Res. Atmos.: Atmos.,* https://doi.org/10.1029/2009JD011760

Oltmans, S. J., Johnson, B. J., Harris, J. M., Vömel, H., Thompson, A. M., et al. (2001). Ozone in the Pacific tropical troposphere from ozonesonde observations*, J. Geophys. Res. Atmos.,* 106, 32503-32526, doi: https://doi.org/10.1029/2000JD900834

Pan, X., Chin, M., Ichoku, C. M., Field, R. D. (2018) Connecting Indonesian fires and drought with the type of El Niño and phase of the Indian Ocean Dipole during 1979–2016, *J. Geophys. Res. Atmos.,* https://doi.org/10.1029/2018JD028402

Randel, W. J., Park, M., Wu, F. (2007). A large annual cycle in ozone above the tropical tropopause linked to the Brewer–Dobson circulation, *J. Atmos. Sci.*, 64, 4479-4488, doi: 10.1175/2007JAS2409.1

Randel, W. J., and Thompson, A. M. (2011), Interannual variability and trends in tropical ozone derived from SHADOZ ozonesondes and SAGE II satellite data, *J. Geophys. Res. Atmos.*, 116, D07303, doi:10.1029/ 2010JD015195

Selkirk, H. B., Vömel, H., Valverde Canossa, J. M., Pfister, L., Diaz, J. A., Fernández, W., et al. (2010) Detailed structure of the tropical upper troposphere and lower stratosphere as revealed by balloonsonde observations of water vapor, ozone, temperature and winds during the NASA TCSP and TC^4 Campaigns, *J. Geophys. Res. Atmos.*, 115, https://doi.org/10.1029/2009JD013209

SPARC/IO3C/GAW (2019). SPARC/IO3C/GAW Report on Long-term Ozone Trends and Uncertainties in the Stratosphere, I. Petropavlovskikh, S. Godin-Beekmann, D. Hubert, R. Damadeo, B. Hassler, V. Sofieva (Eds.), SPARC Report No. 9, GAW Report No. 241, WCRP-17/2018, doi: 10.17874/f899e57a20b; www.sparc-climate.org/publications/sparc-reports

Stauffer, R. M., Thompson, A. M., Young, G. S. (2016) Free tropospheric ozonesonde profiles at long-term U.S. monitoring sites: 1. A climatology based on self-organizing maps, *J. Geophys. Res. Atmos., 121*, doi: 10.1002/ 2015JD023641

Stauffer, R. M., Thompson, A. M., Witte, J. C. (2018). Characterizing global ozonesonde profile variability from surface to the UT/LS with a clustering technique and MERRA-2 reanalysis, *J. Geophys. Res. Atmos. Atmos*., 123, 6213–6229, https://doi.org/10.1029/2018JD028465

Stauffer, R. M., Thompson, A. M., Kollonige, D. E., Witte, J. C., Tarasick, D. W., Davies, J., et al. (2020). A post-2013 dropoff in total ozone at a third of global ozonesonde stations: Electrochemical concentration cell instrument artifacts? *Geophys. Res. Lett*., 47, e2019GL086791. https://doi.org/10.1029/2019GL086791

Stauffer, R. M., Thompson, A. M., Oman, L. D., Strahan, S. E. (2019) The effects of a changing observing system on MERRA-2-based ozone profile simulations (1980-2016), *J. Geophys. Res. Atmos., 124,* doi: 10.1002/2018JD030090

Sterling, C. W., Johnson, B. J., Oltmans, S. J., Smit, H. G. J., Jordan, A. F., Cullis, P. D., et al. (2018). Homogenizing and estimating the uncertainty in NOAA's long-term vertical ozone profile records measured with the electrochemical concentration cell ozonesonde, *Atmos. Meas. Tech*., 11, 3661-3687, https://doi.org/10.5194/amt-11-3661-2018

Stolarski, R. S., Bloomfield, P. R., McPeters, R. D., Herman, J. R. (1991). Total ozone trends deduced from Nimbus 7 TOMS data, *Geophys. Res. Lett*., 18, 1015-1018, https://doi.org/10.1029/91GL01302

Stolarski, R. S., Waugh, D. W., Wang, L., Oman, L. D., Douglass, A. R., Newman, P. A. (2014). Seasonal variation of ozone in the tropical lower stratosphere: Southern tropics are different from northern tropics, *J. Geophys. Res. Atmos*., 119, 6196–6206, doi:10.1002/2013JD021294

Swap, R. J., Annegarn, H. J., Suttles, J. T., Haywood, J., Hemlinger, M. C., et al., (2002). The Southern African Regional Science Initiative (SAFARI-2000): Dry-Season Campaign, an Overview, *S. Afr. J. Science*, 98, 125-130

Szeląg, M. E., Sofieva, V. F., Degenstein, D., Roth, C., Davis, S., and Froidevaux, L. (2020). Seasonal stratospheric ozone trends over 2000–2018 derived from several merged data sets, *Atmos. Chem. Phys*., 20, 7035–7047, https://doi.org/10.5194/acp-20-7035-2020

Thompson, A. M., and Hudson, R. D. (1999) Tropical Tropospheric Ozone (TTO) maps from Nimbus-7 and Earth-Probe TOMS by the modified-residual method: Evaluation with sondes, ENSO signals and trends from Atlantic regional time series, *J. Geophys. Res. Atmos.,* 26,961-26,975

Thompson, A. M., Witte, J. C., Hudson, R. D., Guo, H., Herman, J. R., Fujiwara, M. (2001) Tropical tropospheric ozone and biomass burning, *Science,* 291, 2128-2132

Thompson, A. M., Witte, J. C., McPeters, R. D., Oltmans, S. J., Schmidlin, F. J., J. A. Logan, J. A., et al. (2003a) Southern Hemisphere ADditional Ozonesondes (SHADOZ) 1998-2000 tropical ozone climatology. 1. Comparison with TOMS and ground-based measurements*, J. Geophys. Res. Atmos.,* 108, 8238, doi: 10.1029/2001JD000967

669 Thompson, A. M., Witte, J. C., Oltmans, S. J., Schmidlin, F. J., Logan, J. A., et al. (2003b) Southern
670 Hemisphere ADditional Ozonesondes (SHADOZ) 1998-2000 tropical ozone climatology. 2. Tropospheric
671 Variability and the zonal wave-one, *J. Geophys. Res. Atmos.,* 108, 8241, doi:
672 https://doi.org/10.1029/2002JD002241

673 Thompson, A. M., Allen, A. L., Lee, S. Miller, S. K., Witte, J. C. (2011). Gravity and Rossby wave
674 signatures in the tropical troposphere and lower stratosphere based on Southern Hemisphere Additional
675 Ozonesondes (SHADOZ), 1998–2007, *J. Geophys. Res. Atmos.*, 116, D05302, doi:10.1029/2009JD013429

676 Thompson, A. M., Miller, S. K., Tilmes, S., Kollonige, D. W., Witte, J. C., et al. (2012). Southern
677 Hemisphere Additional Ozonesondes (SHADOZ) tropical ozone climatology: Tropospheric and tropical
678 tropopause layer (TTL) profiles with comparisons to OMI based ozone products. *J. Geophys. Res. Atmos.*,
679 117, D23301, doi: 10.1029/2010JD016911

680 Thompson, A. M., Witte, J. C., Sterling, C., Jordan, A., Johnson, B. J., Oltmans, S. J., et al. (2017). First
681 reprocessing of Southern Hemisphere Additional Ozonesondes (SHADOZ) ozone profiles (1998–2016): 2.
682 Comparisons with satellites and ground-based instruments, *J. Geophys. Res. Atmos*., 122, 13,000–13,025,
683 https://doi.org/10.1002/2017JD027406

684 Thouret, V., Saunois, M., Minga, A., Mariscal, A., Sauvage, B., Solete, A., et al. (2009) An overview of two
685 years of ozone radio soundings over Cotonou as part of AMMA, *Atmos. Chem. Phys.,* 9, 6157–6174,
686 https://doi.org/10.5194/acp-9-6157-2009

687 Wargan, K., Orbe, C., Pawson, S., Ziemke, J. R., Oman, L. D., Olsen, M. A., et al. (2018). Recent decline in
688 extratropical lower stratospheric ozone attributed to circulation changes, *Geophys. Res. Lett*., 45, 5166–
689 5176, https://doi.org/10.1029/2018GL077406

690 Wilks, D.S. (1997). Resampling hypothesis tests for autocorrelated fields, *J. Climate*, 10 (1), 65-82,
691 https://doi.org/10.1175/1520-0442(1997)010<0065:RHTFAF>2.0.CO;2

692 Witte, J. C., Schoeberl, M. R., Douglass, A. R., Thompson, A. M. (2008) The Quasi-biennial Oscillation in
693 tropical ozone from SHADOZ and HALOE, *Atmos. Chem. Phys.,* 8, 6355-6378

694 Witte, J. C., Thompson, A. M., Smit, H. G. J., Fujiwara, M., Posny, F., et al. (2017). First reprocessing of
695 Southern Hemisphere ADditional Ozonesondes (SHADOZ) profile records (1998-2015): 1. Methodology
696 and evaluation, *J. Geophys. Res. Atmos*., 122, doi:10.1002/2016JD026403

697 Witte, J. C., Thompson, A. M., Smit, H. G. J., Fujiwara, M., Johnson, B. J., et al. (2018). First reprocessing
698 of Southern Hemisphere ADditional Ozonesondes (SHADOZ) profile records (1998-2016): 3.
699 Methodology and evaluation, *J. Geophys. Res. Atmos*., 123, doi:10.1002/2017JD027791

700 Zhang, Y. Cooper, O. R., Gaudel, A., Thompson, A. M., Nédelec, P., Ogino, S.-Y., West, J. J. (2016).
701 Equatorward redistribution of emissions dominates the 1980 to 2010 tropospheric ozone change,
702 *Nature-Geoscience*, doi: 10.1038/NGEO2827

703 Ziemke, J. R., and Chandra, S. (2003) A Madden-Julian Oscillation in tropospheric ozone, *Geophys. Res.,*
704 *Lett.,* https://doi.org/10.1029/2003GL018523

705 Ziemke, J. R., Chandra, S., Duncan, B. N., Froidevaux, L., Bhartia, P. K., Levelt, P. F., Waters, J. W. (2006).
706 Tropospheric ozone determined from Aura OMI and MLS: Evaluation of measurements and comparison
707 with the Global Modeling Initiative's Chemical Transport Model, *J. Geophys. Res.,* 111, D19303,
708 https://doi.org/10.1029/2006JD007089.

709 Ziemke, J. R., Oman, L. D., Strode, S. A., Douglass, A. R., Olsen, M. A., et al. (2019). Trends in Global
710 Tropospheric Ozone Inferred from a Composite Record of TOMS/OMI/MLS/OMPS Satellite
711 Measurements and the MERRA-2 GMI Simulation, *Atmos. Chem. Phys*. 19, 3257–3269, doi:
712 https://doi.org/10.5194/acp-19-3257-2019

Table Labels and Figure Captions

Table 1. SHADOZ site metadata including number of profiles and index terms used in MLR ozone calculations. Monthly MLR partial column ozone linear trends are shown in percent per decade and include the 95% confidence interval and p-value for each trend. Trends with p-values <0.05 are shown in bold and underlined.

Table 2. Same as Table 1, with SHADOZ site metadata and index terms used in MLR ozone calculations. Here the MLR partial column ozone linear trends, in %/decade, are based on FT columns referenced to the tropopause height (TH) -5 km to TH – 10 km, for the lower FT, and for the upper FT, the ozone column between the TH and 5 km below the TH. The LMS column ozone is defined by integrating ozone in the region between the TH and 5 km above it. **Table T2** gives the same trends information in DU/decade.

Figure 1. Map of SHADOZ stations used in this study. Stations whose combined records are examined are colored orange (San Cristóbal and Paramaribo), red (Natal and Ascension), and blue (Kuala Lumpur and Watukosek). Samoa and Nairobi records are studied individually and colored gray. Sample numbers appear in **Table 1.**

Figure 2. Monthly averaged ozone mixing ratios from the surface to 20 km altitude for the five sites: two individual and three combinations. For clarity both white and black contours are used for the ozone mixing ratios. White dashed lines indicate transition periods marked by changes in sign of ozone anomalies from annual mean (see Figure 4).

Figure 3. Seasonal ozone variability, expressed as percent anomaly from annual mean, from the MLR model in the LMS (a), FT (b and c). Tropopause Height (TH) anomaly (d, in km) is based on the 380 K potential temperature surface from the radiosondes.

Figure 4. Monthly averaged O_3 mixing ratio anomalies in percent from the annual mean from the surface to 20 km altitude for the two individual and three combination sites. Black dashed lines (same as the white dashed lines in **Figure 2**) indicate transition periods marked by sign changes to the climatological FT and LMS O_3 amounts (see Section 3.1).

Figure 5. Monthly averaged gravity wave frequency (GWF) in percent from 10 to 20 km altitude corresponding to the profiles in Figure 2 for the two individual and three combination sites. White dashed lines are set by the ozone seasonal transitions as shown as in **Figures 2 and 4.** The GWF frequency is computed by determining GW effects in percent for each individual profile, and then averaging the results into a monthly frequency.

Figure 6. Monthly MLR ozone linear trends from 5 to 20 km in percent per decade for the two individual and three combination sites. Positive trends are shown in red and negative trends are shown in blue. Trends with p-values <0.05 are shown with cyan hatching.

Figure 7. Monthly MLR trends in %/decade for (a) lower FT ozone column, integrated from 5-10 km, and (b) upper FT ozone column (10-15 km), derived from SHADOZ sondes. Dots represent the values and the error bars indicate the 95% confidence intervals. **Table 1** shows

759 that the annually averaged trend for Nat-Asc at 10-15 km is the only one with $p \leq 0.05$. Note in
760 (b) that the Nat-Asc monthly trends are generallylower than for the other 4 stations in February
761 to May. However, the Nat-Asc ozone increases alone are sustained from June into September.
762
763 **Figure 8**. Cluster ozone means for the two individual and three combination sites for SOM
764 Cluster 1 (a) and Cluster 4 (b). The number and percentage of profiles contributing to the
765 clusters appear in each frame and the Cluster number is at the lower right. Note that SOM for
766 Clusters 2 and 3 are not shown. (c, d): Gravity wave frequency (GWF in text) as a function of
767 altitude corresponding to SOM Clusters 1 and 4. Average percentage GWF from 15 to 20 km
768 (LMS) for each site is shown in the frames. (e) Monthly frequency distribution for the profiles
769 corresponding to SOM Cluster 1. (f) as (e) for Cluster 4.
770
771 **Figure 9.** Change in monthly GWF over two periods (2015-2019 minus 1998-2002) from 10 to
772 20 km altitude. Increases in GWF are shown in red and decreases in GWF are shown in blue for
773 the two individual and three combination sites.
774
775 **Figure 10**. Monthly MLR trends, as %/decade ($\pm$ 1σ), in (a) LMS ozone column changes (15-20
776 km) derived from SHADOZ sondes at 5 stations; (b) corresponding TH trends from the
777 radiosondes. Dots represent the values and the error bars indicate the 95% confidence
778 intervals.
779
780 **Figure 11**. Monthly MLR trends in LMS ozone column changes, as %/decade ($\pm$ 1σ), derived
781 from SHADOZ sondes at 5 stations, where the LMS column is defined by the amount between the
782 altitude of the tropopause and the tropopause + 5km.
783
784

Table 1. SHADOZ site metadata including number of profiles and index terms used in MLR ozone calculations. Monthly MLR partial column ozone linear trends are shown in percent per decade and include the 95% confidence interval and p-value for each trend. Trends with p-values <0.05 are shown in bold and underlined.

Trends by layer, % per decade																
Site	**Lat, Lon (°)**	**Profiles**	**MLR Terms and Alt.**	**Jan**	**Feb**	**Mar**	**Apr**	**May**	**Jun**	**Jul**	**Aug**	**Sep**	**Oct**	**Nov**	**Dec**	**Ann**
SC+Para	-0.92, -89.62/5.8, -55.21	1227	MEI+QBO													
			5-10 km	-5.0±8.4% p = 0.233	1.4±9.1% p = 0.764	**8.1±8.1% p = 0.050**	6.4±8.4% p = 0.121	-0.0±10.0% p = 0.995	-1.1±8.8% p = 0.808	1.8±7.4% p = 0.609	3.0±6.5% p = 0.345	3.1±5.8% p = 0.271	4.2±6.3% p = 0.183	2.8±7.3% p = 0.435	-2.7±7.5% p = 0.470	1.9±3.1% p = 0.079
			10-15 km	-7.7±11.1% p = 0.162	-5.6±11.8% p = 0.336	4.8±10.8% p = 0.361	12.3±12.4% p = 0.055	4.4±13.4% p = 0.511	-3.1±10.0% p = 0.540	-0.3±8.6% p = 0.942	6.0±8.4% p = 0.155	6.7±7.6% p = 0.081	3.8±8.0% p = 0.343	0.5±8.9% p = 0.904	-3.2±9.3% p = 0.487	1.5±4.0% p = 0.260
			15-20 km	-1.5±9.1% p = 0.733	0.8±9.0% p = 0.848	2.9±8.1% p = 0.456	1.9±8.0% p = 0.623	-1.6±8.1% p = 0.688	-4.1±7.0% p = 0.231	-5.2±5.6% p = 0.070	**-6.1±5.1% p = 0.020**	**-6.5±5.2% p = 0.013**	-5.5±5.8% p = 0.060	-3.7±6.7% p = 0.265	-2.4±7.8% p = 0.517	**-3.1±2.8% p = 0.021**
Natal+Ascen	-5.42, -35.38/-7.58, -14.24	1436	MEI+QBO													
			5-10 km	2.6±5.7% p = 0.357	2.2±5.8% p = 0.445	2.1±6.0% p = 0.471	3.9±7.4% p = 0.283	7.2±8.1% p = 0.078	**7.4±7.1% p = 0.036**	4.7±6.1% p = 0.114	0.5±5.3% p = 0.850	-2.6±4.7% p = 0.253	-2.8±4.5% p = 0.196	-1.0±4.8% p = 0.668	1.4±5.2% p = 0.560	1.6±2.3% p = 0.143
			10-15 km	6.7±7.2% p = 0.059	**7.7±7.5% p = 0.042**	4.9±8.0% p = 0.198	2.4±9.9% p = 0.595	3.6±9.5% p = 0.423	6.1±7.6% p = 0.100	**7.1±7.0% p = 0.044**	5.5±6.6% p = 0.093	2.2±5.7% p = 0.411	0.3±5.3% p = 0.919	0.4±5.8% p = 0.894	3.0±6.3% p = 0.318	**3.9±2.8% p = 0.001**
			15-20 km	2.2±6.1% p = 0.454	4.5±6.8% p = 0.177	3.1±6.9% p = 0.341	3.4±7.5% p = 0.329	5.2±7.7% p = 0.159	1.4±6.8% p = 0.639	-3.8±5.5% p = 0.146	**-5.2±4.9% p = 0.040**	-2.9±4.9% p = 0.215	-1.6±5.0% p = 0.502	-2.6±5.1% p = 0.297	-1.8±5.4% p = 0.477	-0.4±2.4% p = 0.528
Nairobi	-1.27, 36.8	941	MEI+QBO													
			5-10 km	2.0±8.1% p = 0.639	**10.1±8.7% p = 0.018**	**14.2±8.7% p = 0.001**	6.1±8.2% p = 0.140	-3.8±7.2% p = 0.297	-5.0±6.4% p = 0.125	-1.3±7.0% p = 0.701	0.0±7.5% p = 0.997	-1.5±7.1% p = 0.679	-1.1±7.1% p = 0.769	0.4±7.6% p = 0.923	0.0±7.6% p = 0.991	1.2±3.1% p = 0.119
			10-15 km	0.1±9.5% p = 0.979	4.5±10.1% p = 0.350	8.8±9.1% p = 0.059	7.4±8.8% p = 0.093	2.1±8.5% p = 0.615	0.1±8.3% p = 0.989	0.9±9.7% p = 0.838	-2.3±9.5% p = 0.603	-7.0±7.5% p = 0.062	**-6.8±6.2% p = 0.035**	-3.3±6.3% p = 0.271	-1.0±7.3% p = 0.780	-0.2±3.4% p = 0.707
			15-20 km	3.1±6.9% p = 0.376	5.5±7.7% p = 0.152	7.3±7.9% p = 0.066	6.0±7.5% p = 0.110	1.2±6.9% p = 0.736	-3.3±5.7% p = 0.242	-4.3±5.0% p = 0.089	-2.9±4.9% p = 0.249	-0.9±5.1% p = 0.742	0.2±5.6% p = 0.940	0.6±6.4% p = 0.853	1.4±6.5% p = 0.670	0.6±2.5% p = 0.553
KL+Java	2.73, 101.27/-7.5, 112.6	786	MEI+QBO+IOD													
			5-10 km	-0.2±6.8% p = 0.947	**12.9±7.5% p = 0.001**	**15.7±8.2% p = 0.000**	3.9±7.1% p = 0.267	-3.0±6.2% p = 0.327	-2.5±6.5% p = 0.441	0.0±7.4% p = 0.991	1.8±8.2% p = 0.665	3.9±7.7% p = 0.317	3.3±7.0% p = 0.353	-1.7±7.4% p = 0.660	-6.0±7.3% p = 0.102	1.9±3.0% p = 0.138
			10-15 km	-2.8±7.5% p = 0.456	2.8±7.6% p = 0.466	**12.9±9.2% p = 0.005**	**15.1±8.5% p = 0.000**	5.2±6.9% p = 0.133	-4.5±6.6% p = 0.173	-7.6±7.7% p = 0.053	-3.3±10.0% p = 0.500	-1.5±9.4% p = 0.757	-4.7±7.8% p = 0.231	-6.6±8.5% p = 0.120	-5.9±8.8% p = 0.180	-0.6±3.3% p = 0.347
			15-20 km	**-8.8±7.1% p = 0.015**	-4.4±8.3% p = 0.289	-0.6±8.1% p = 0.898	1.1±8.3% p = 0.795	-0.2±7.5% p = 0.942	-4.6±6.0% p = 0.122	**-9.0±5.5% p = 0.001**	**-9.3±5.5% p = 0.001**	**-6.0±5.6% p = 0.035**	-4.8±6.7% p = 0.151	**-7.8±7.7% p = 0.043**	**-10.0±7.0% p = 0.005**	**-5.8±2.8% p = 0.000**
Samoa	-14.23, -170.56	795	MEI+QBO													
			5-10 km	7.2±12.3% p = 0.245	6.3±12.9% p = 0.322	6.0±14.5% p = 0.400	2.1±14.7% p = 0.770	-1.3±11.8% p = 0.822	-0.6±10.6% p = 0.912	0.4±11.1% p = 0.947	-2.5±10.8% p = 0.629	-5.1±9.9% p = 0.297	-2.4±9.7% p = 0.624	3.9±10.5% p = 0.460	7.7±11.9% p = 0.191	1.4±4.7% p = 0.226
			10-15 km	7.3±19.5% p = 0.448	15.0±20.8% p = 0.147	16.5±21.2% p = 0.123	12.0±22.0% p = 0.275	2.3±16.3% p = 0.780	-2.3±12.8% p = 0.720	-1.8±13.0% p = 0.779	1.4±13.8% p = 0.841	1.7±13.9% p = 0.808	-2.1±14.5% p = 0.778	-4.2±14.5% p = 0.562	-1.1±15.4% p = 0.878	2.5±6.5% p = 0.243
			15-20 km	-3.8±8.6% p = 0.377	0.4±9.3% p = 0.929	-0.4±9.8% p = 0.926	-5.9±10.2% p = 0.244	-6.4±9.7% p = 0.179	-2.1±9.0% p = 0.641	-0.4±8.4% p = 0.924	-2.3±7.4% p = 0.525	-3.1±6.9% p = 0.369	-2.2±7.1% p = 0.537	-2.9±7.4% p = 0.427	-5.0±7.8% p = 0.198	-2.8±3.4% p = 0.115

Table 2. Same as Table 1, with SHADOZ site metadata and index terms used in MLR ozone calculations. Here the MLR partial column ozone linear trends, in %/decade, are based on FT columns referenced to the tropopause height (TH) -5 km to TH – 10 km, for the lower FT, and for the upper FT, the ozone column between the TH and 5 km below the TH. The LMS column ozone is defined by integrating ozone in the region between the TH and 5 km above it. **Table T2** gives the same trends information in DU/decade.

Trends by layer, % per decade																
Site	**Lat, Lon (°)**	**Profiles**	**MLR Terms and Alt.**	**Jan**	**Feb**	**Mar**	**Apr**	**May**	**Jun**	**Jul**	**Aug**	**Sep**	**Oct**	**Nov**	**Dec**	**Ann**
SC+Para	-0.92, -89.62/5.8, -55.21	1227	MEI+QBO													
			TH-10 to TH-5 km	-7.9±8.9% p = 0.076	-2.3±9.7% p = 0.624	6.0±9.0% p = 0.184	5.5±9.5% p = 0.242	-0.4±10.4% p = 0.939	-0.8±8.5% p = 0.841	0.9±7.0% p = 0.809	-0.0±6.4% p = 0.999	-0.6±5.6% p = 0.846	1.5±6.2% p = 0.626	1.8±7.3% p = 0.607	-3.8±7.6% p = 0.309	-0.1±3.2% p = 0.905
			TH-5 km to TH	-8.9±11.7% p = 0.127	-5.4±12.2% p = 0.373	5.2±11.5% p = 0.365	9.5±12.6% p = 0.134	1.7±12.5% p = 0.787	-2.3±10.1% p = 0.648	0.7±8.9% p = 0.878	3.7±8.5% p = 0.386	2.6±7.9% p = 0.505	1.1±8.9% p = 0.801	-0.1±10.1% p = 0.977	-4.3±10.1% p = 0.396	0.2±4.2% p = 0.875
			TH to TH+5 km	-0.6±6.2% p = 0.831	0.8±5.9% p = 0.783	2.0±5.3% p = 0.434	2.6±5.5% p = 0.328	2.3±6.3% p = 0.455	1.6±6.3% p = 0.608	1.2±5.8% p = 0.658	1.0±5.5% p = 0.728	0.2±5.3% p = 0.933	-0.8±5.3% p = 0.747	-1.6±5.2% p = 0.545	-1.5±5.4% p = 0.580	0.6±2.3% p = 0.428
Natal+Ascen	-5.42, -35.38/-7.58, -14.24	1436	MEI+QBO													
			TH-10 to TH-5 km	3.6±6.4% p = 0.239	3.4±6.6% p = 0.275	1.9±6.6% p = 0.542	3.8±8.4% p = 0.329	**9.7±9.0% p = 0.034**	**9.9±7.3% p = 0.013**	5.7±6.1% p = 0.064	1.0±5.5% p = 0.673	-1.9±4.9% p = 0.416	-2.9±4.7% p = 0.194	-2.3±5.0% p = 0.324	0.4±5.7% p = 0.878	2.0±2.5% p = 0.073
			TH-5 km to TH	**8.0±6.7% p = 0.021**	**10.1±7.6% p = 0.010**	6.4±7.8% p = 0.097	4.0±9.3% p = 0.363	5.7±8.9% p = 0.191	6.6±7.2% p = 0.066	6.2±6.4% p = 0.061	5.5±6.1% p = 0.074	3.8±5.5% p = 0.162	1.4±5.2% p = 0.572	0.2±5.4% p = 0.950	2.6±5.6% p = 0.333	**4.7±2.7% p = 0.000**
			TH to TH+5 km	3.2±4.7% p = 0.154	4.9±5.0% p = 0.051	4.2±4.9% p = 0.087	2.7±4.9% p = 0.270	2.4±5.1% p = 0.332	1.5±5.1% p = 0.535	-0.3±4.7% p = 0.892	-0.8±4.5% p = 0.713	0.7±4.4% p = 0.761	1.8±4.2% p = 0.380	1.5±4.4% p = 0.487	1.5±4.5% p = 0.501	1.9±1.9% p = 0.052
Nairobi	-1.27, 36.8	941	MEI+QBO													
			TH-10 to TH-5 km	-1.8±9.9% p = 0.719	4.5±10.2% p = 0.374	**10.1±9.7% p = 0.036**	5.8±9.2% p = 0.212	-2.8±8.1% p = 0.495	-4.6±7.3% p = 0.208	-1.5±7.9% p = 0.701	-0.5±8.3% p = 0.896	-2.5±7.8% p = 0.532	-2.0±7.3% p = 0.585	-0.2±7.2% p = 0.955	-1.0±8.1% p = 0.807	-0.0±3.4% p = 0.955
			TH-5 km to TH	0.7±8.8% p = 0.863	5.9±9.8% p = 0.214	**9.2±9.0% p = 0.042**	6.5±8.5% p = 0.125	2.1±8.3% p = 0.604	1.8±7.8% p = 0.651	3.1±8.7% p = 0.448	-0.5±8.8% p = 0.905	-5.5±7.4% p = 0.128	-5.4±6.2% p = 0.081	-2.7±6.3% p = 0.364	-0.9±7.1% p = 0.778	0.7±3.2% p = 0.205
			TH to TH+5 km	6.5±6.7% p = 0.056	2.9±6.7% p = 0.368	-1.4±6.6% p = 0.672	-0.4±6.4% p = 0.885	1.9±6.7% p = 0.550	-0.1±6.8% p = 0.980	-2.5±6.5% p = 0.421	0.1±6.5% p = 0.974	4.5±6.7% p = 0.172	4.4±6.5% p = 0.175	2.7±6.5% p = 0.378	4.7±6.7% p = 0.160	1.9±2.7% p = 0.079
KL+Java	2.73, 101.27/-7.5, 112.6	786	MEI+QBO+IOD													
			TH-10 to TH-5 km	-6.4±7.6% p = 0.092	5.1±8.2% p = 0.215	**14.4±9.0% p = 0.001**	**10.1±8.2% p = 0.015**	0.8±7.2% p = 0.813	-4.8±6.8% p = 0.153	-6.4±7.4% p = 0.082	-4.5±8.9% p = 0.318	0.2±8.5% p = 0.970	0.9±7.5% p = 0.813	-3.3±8.3% p = 0.420	**-8.7±8.4% p = 0.040**	-0.6±3.2% p = 0.306
			TH-5 km to TH	-4.2±8.5% p = 0.317	3.3±8.3% p = 0.418	8.6±9.5% p = 0.072	**16.5±10.1% p = 0.001**	**11.6±7.3% p = 0.003**	-1.1±5.9% p = 0.697	**-12.5±6.6% p = 0.000**	**-13.3±8.4% p = 0.003**	-4.7±9.0% p = 0.301	-6.2±8.6% p = 0.149	**-13.2±8.9% p = 0.004**	**-13.4±9.0% p = 0.004**	-3.2±3.3% p = 0.055
			TH to TH+5 km	1.5±7.1% p = 0.661	1.4±7.1% p = 0.684	-0.3±7.3% p = 0.940	-0.3±7.3% p = 0.934	0.1±7.1% p = 0.965	-1.4±6.6% p = 0.657	-3.1±6.8% p = 0.352	-2.0±7.5% p = 0.567	0.2±7.8% p = 0.947	-0.1±8.0% p = 0.981	-1.5±8.2% p = 0.703	-0.6±7.4% p = 0.868	-0.5±3.0% p = 0.621
Samoa	-14.23, -170.56	795	MEI+QBO													
			TH-10 to TH-5 km	14.3±17.9% p = 0.110	8.5±17.5% p = 0.320	4.2±18.2% p = 0.636	3.8±19.9% p = 0.696	1.9±15.5% p = 0.802	-0.7±12.8% p = 0.921	-1.8±13.1% p = 0.788	-2.0±12.9% p = 0.736	-3.5±11.8% p = 0.542	-4.0±11.8% p = 0.485	0.6±13.2% p = 0.921	9.8±15.8% p = 0.208	1.7±5.9% p = 0.270
			TH-5 km to TH	9.2±19.3% p = 0.345	10.5±20.1% p = 0.297	7.9±19.9% p = 0.424	3.5±21.1% p = 0.735	-3.2±16.6% p = 0.699	-6.1±13.1% p = 0.350	-3.8±13.4% p = 0.563	0.9±14.4% p = 0.902	0.6±14.2% p = 0.932	-4.0±14.2% p = 0.578	-4.4±14.3% p = 0.542	1.4±15.6% p = 0.861	0.2±6.5% p = 0.922
			TH to TH+5 km	0.8±5.4% p = 0.765	1.6±6.2% p = 0.620	1.3±6.7% p = 0.704	0.5±6.8% p = 0.896	-2.0±6.5% p = 0.544	-5.3±6.1% p = 0.083	-5.2±5.9% p = 0.073	-1.5±5.9% p = 0.622	1.4±5.9% p = 0.638	0.3±5.4% p = 0.911	-1.4±5.0% p = 0.574	-0.9±4.9% p = 0.711	-0.9±2.4% p = 0.310

Figure 1.

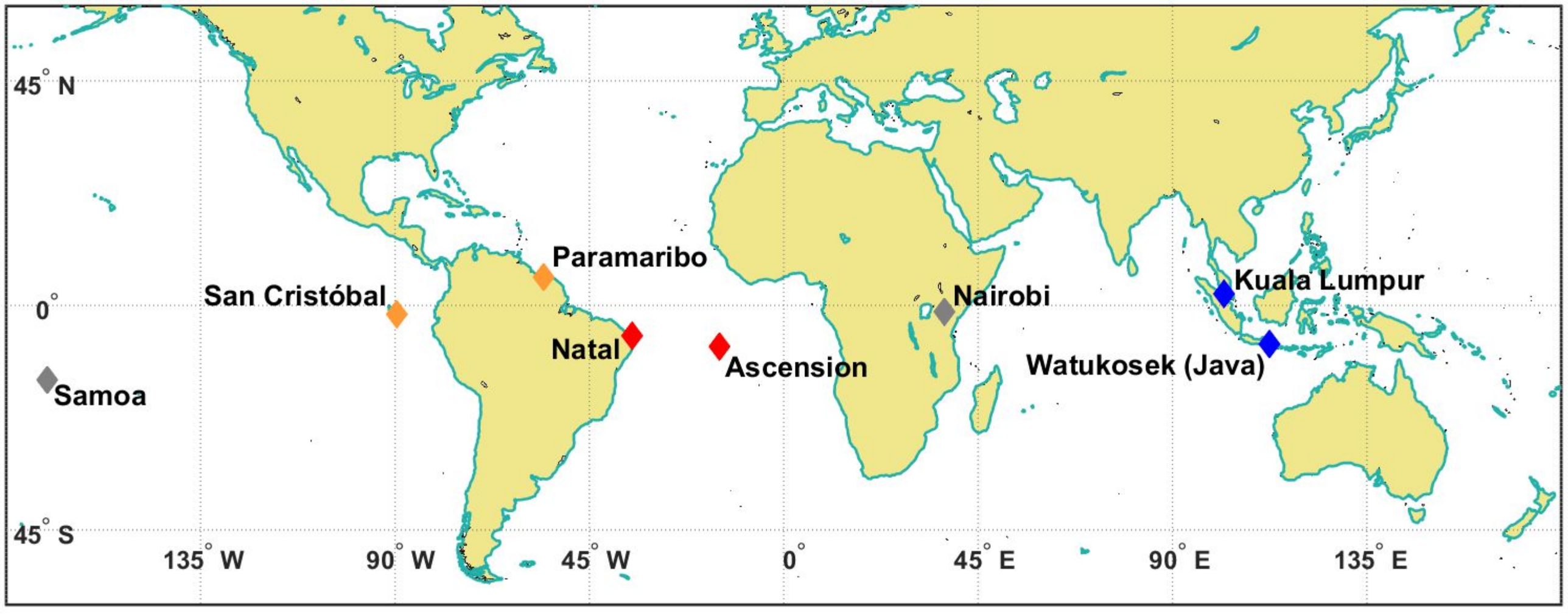
45° N
0°
45° S
135° W
90° W
45° W
0°
45° E
90° E
135° E
Paramaribo
San Cristóbal
Natal
Ascension
Nairobi
Kuala Lumpur
Watukosek (Java)
Samoa

Figure 2.

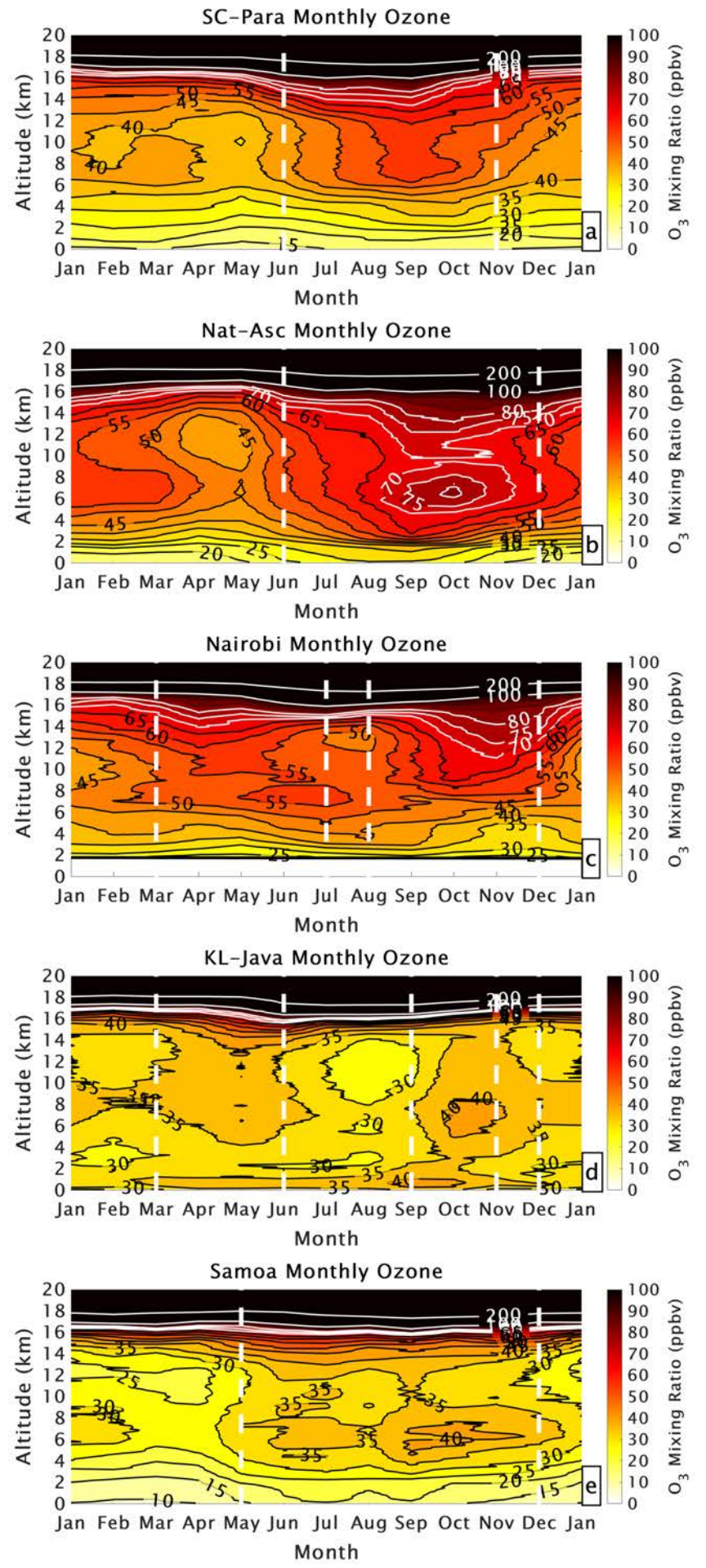
SC-Para Monthly Ozone
Nat-Asc Monthly Ozone
Nairobi Monthly Ozone
KL-Java Monthly Ozone
Samoa Monthly Ozone
Altitude (km)
Month
O3 Mixing Ratio (ppbv)
Jan Feb Mar Apr May Jun Jul Aug Sep Oct Nov Dec Jan
a
b
c
d
e

Figure 3.

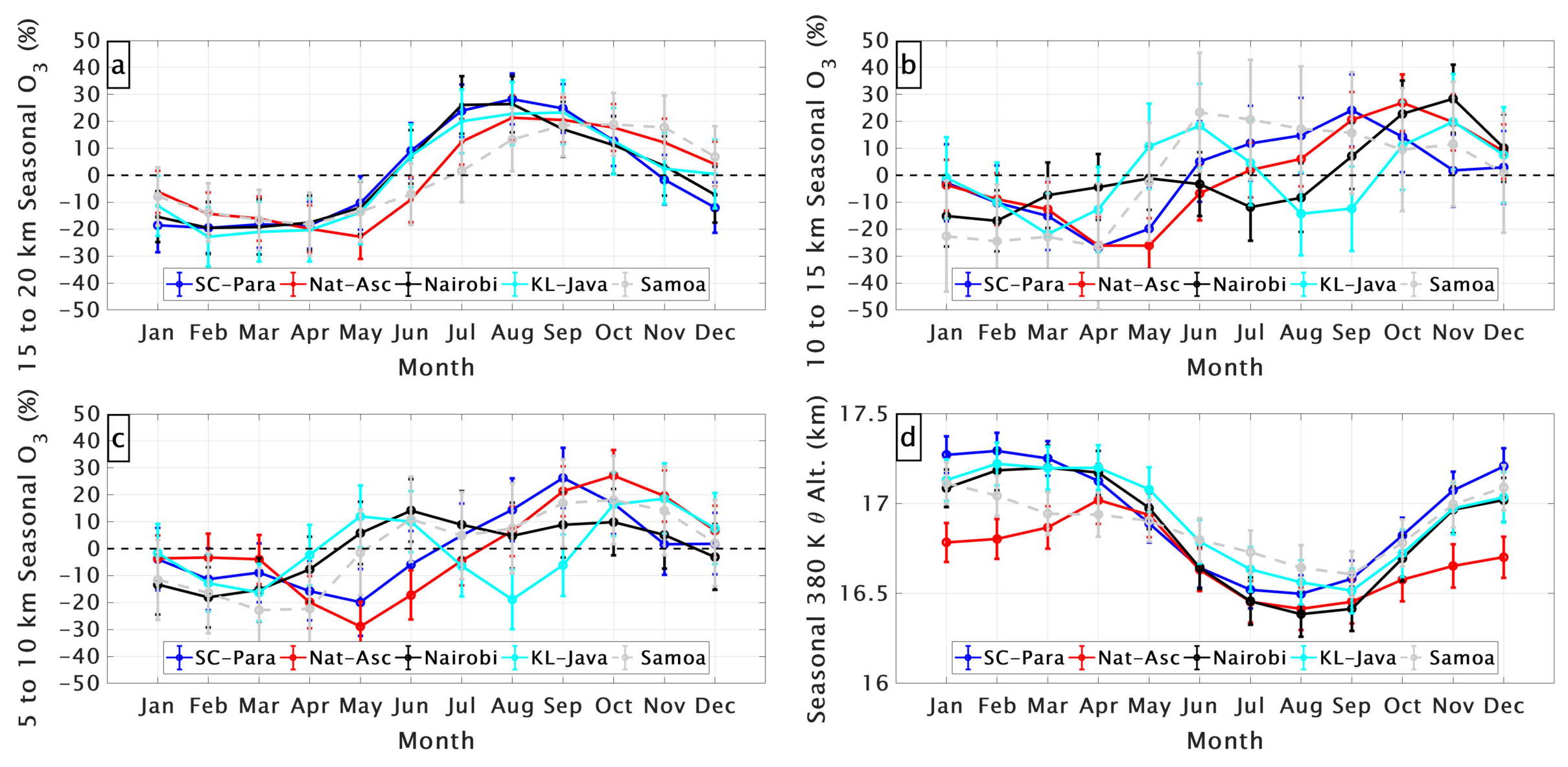
a
b
c
d
15 to 20 km Seasonal O_3 (%)
10 to 15 km Seasonal O_3 (%)
5 to 10 km Seasonal O_3 (%)
Seasonal 380 K θ Alt. (km)
50
40
30
20
10
0
−10
−20
−30
−40
−50
17.5
17
16.5
16
Jan Feb Mar Apr May Jun Jul Aug Sep Oct Nov Dec
Month
SC−Para
Nat−Asc
Nairobi
KL−Java
Samoa

Figure 4.

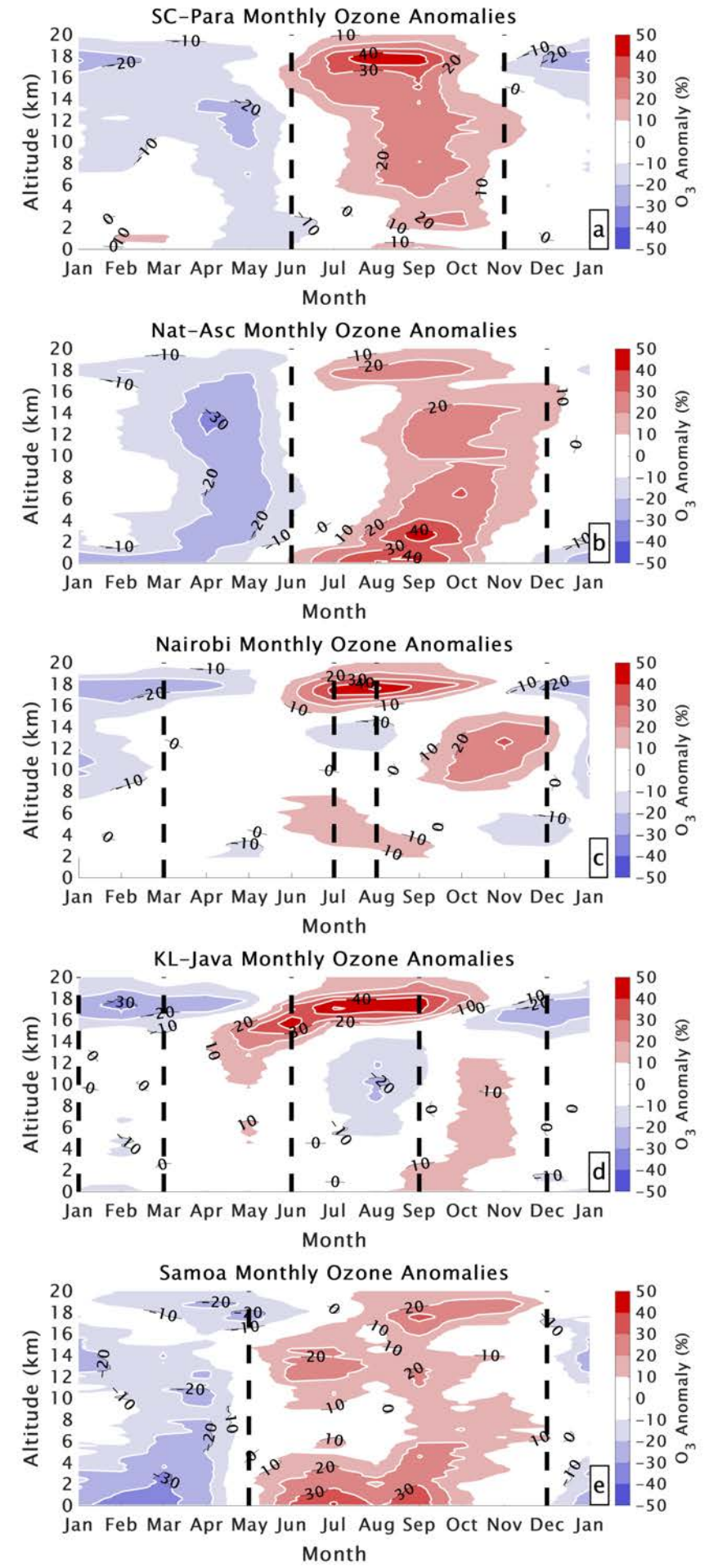
SC-Para Monthly Ozone Anomalies
Nat-Asc Monthly Ozone Anomalies
Nairobi Monthly Ozone Anomalies
KL-Java Monthly Ozone Anomalies
Samoa Monthly Ozone Anomalies
Altitude (km)
Month
Jan Feb Mar Apr May Jun Jul Aug Sep Oct Nov Dec Jan
O3 Anomaly (%)
a
b
c
d
e

Figure 5.

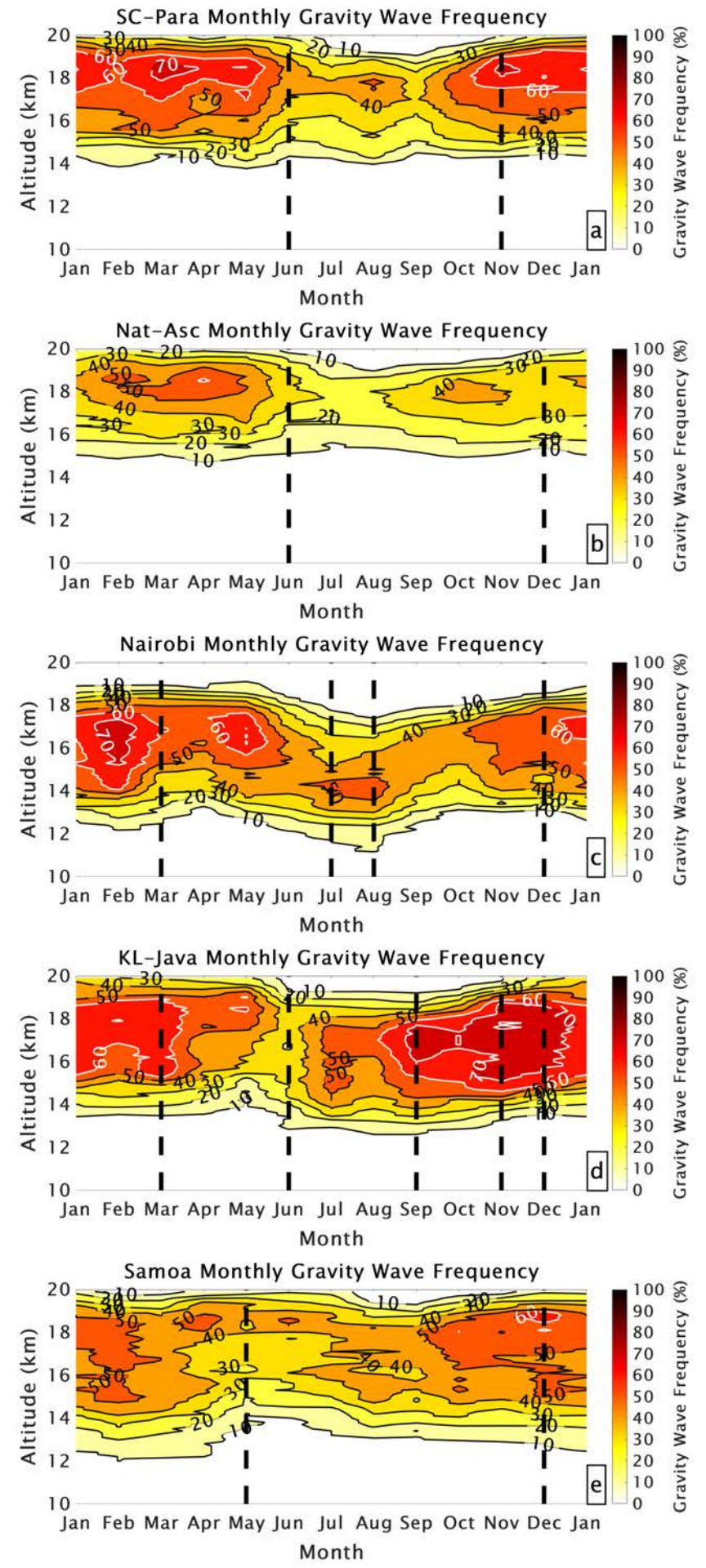
SC-Para Monthly Gravity Wave Frequency
Nat-Asc Monthly Gravity Wave Frequency
Nairobi Monthly Gravity Wave Frequency
KL-Java Monthly Gravity Wave Frequency
Samoa Monthly Gravity Wave Frequency
Altitude (km)
Month
Gravity Wave Frequency (%)
Jan Feb Mar Apr May Jun Jul Aug Sep Oct Nov Dec Jan
a
b
c
d
e

Figure 6.

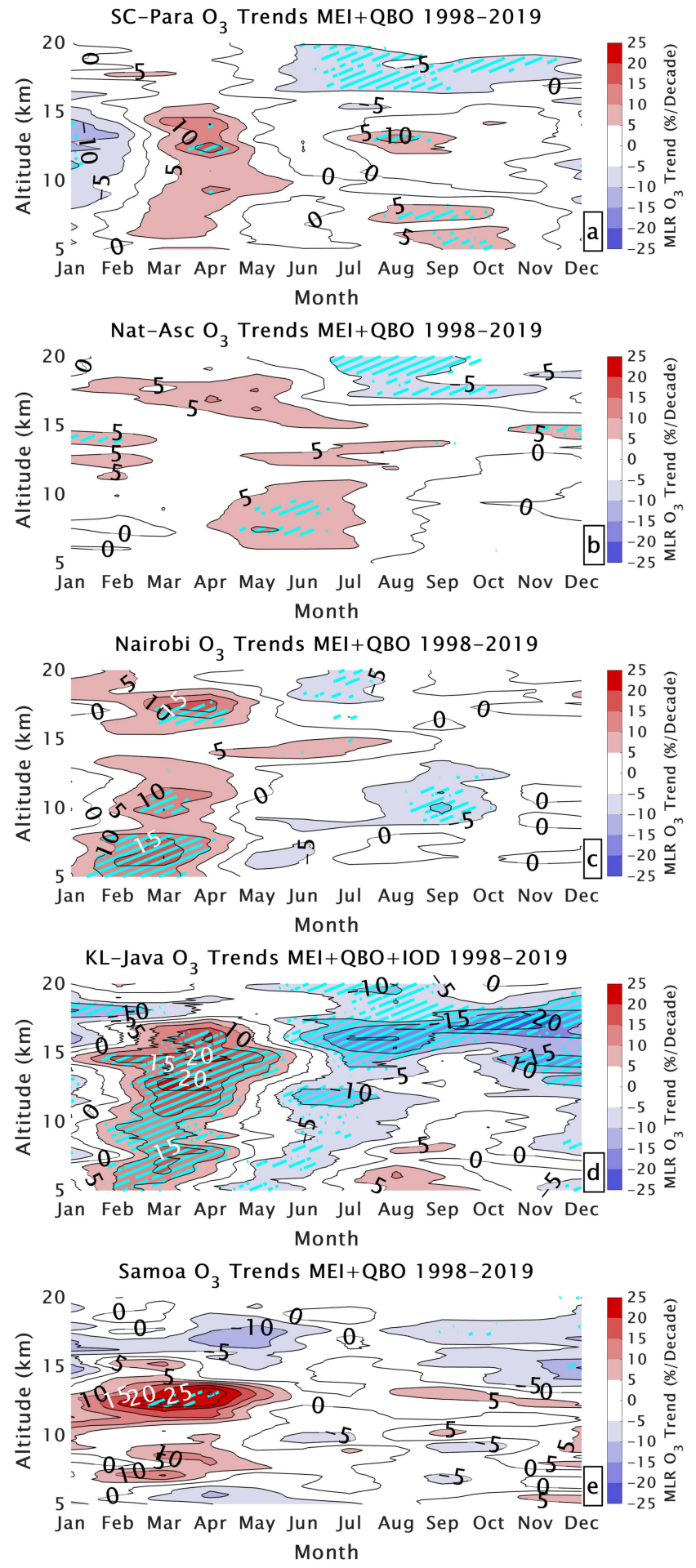
SC-Para O_3 Trends MEI+QBO 1998-2019
Nat-Asc O_3 Trends MEI+QBO 1998-2019
Nairobi O_3 Trends MEI+QBO 1998-2019
KL-Java O_3 Trends MEI+QBO+IOD 1998-2019
Samoa O_3 Trends MEI+QBO 1998-2019
Altitude (km)
Month
Jan Feb Mar Apr May Jun Jul Aug Sep Oct Nov Dec
MLR O_3 Trend (%/Decade)
a
b
c
d
e

Figure 7.

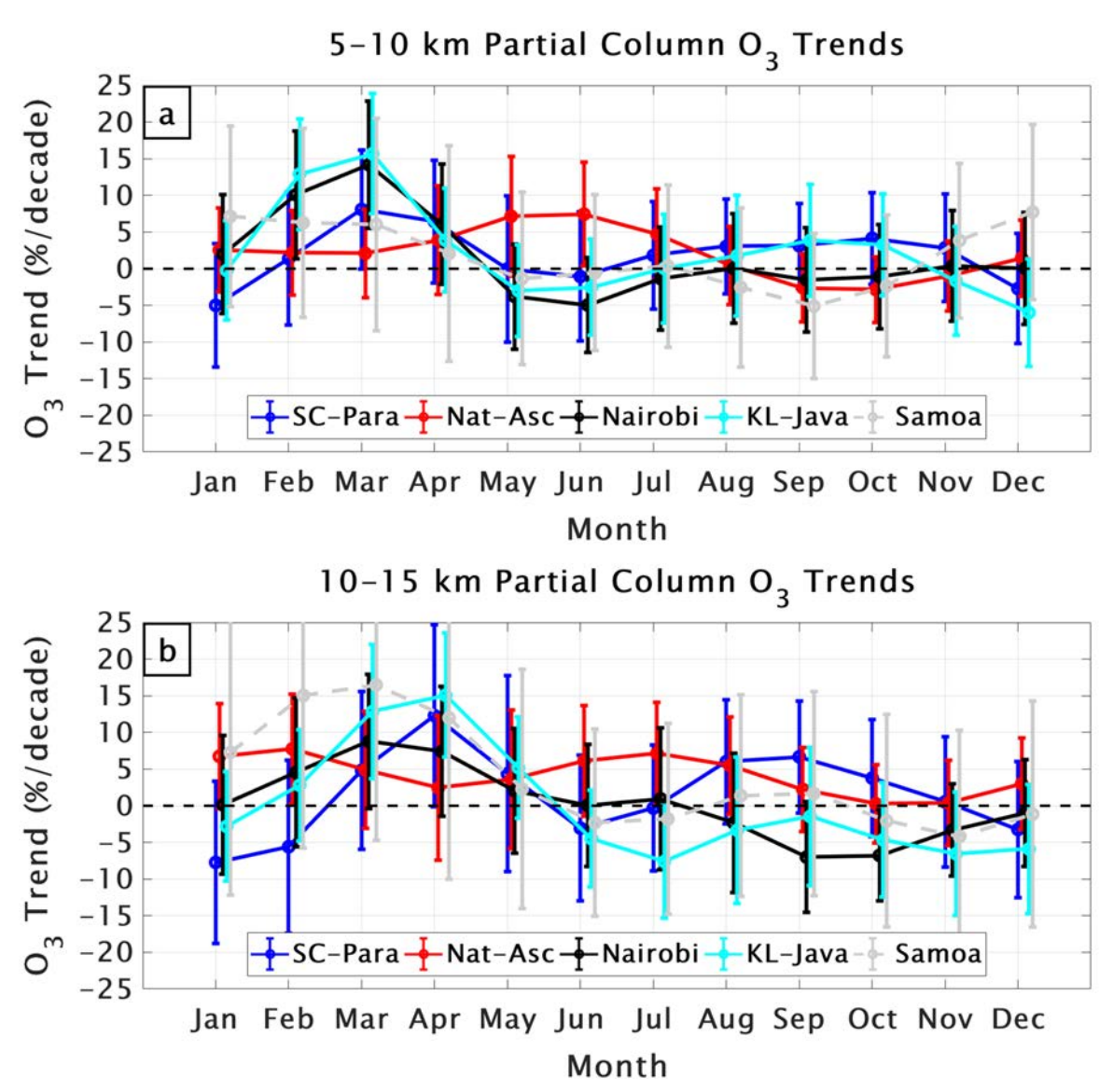
5–10 km Partial Column O_3 Trends
a
O_3 Trend (%/decade)
25
20
15
10
5
0
−5
−10
−15
−20
−25
SC–Para
Nat–Asc
Nairobi
KL–Java
Samoa
Jan
Feb
Mar
Apr
May
Jun
Jul
Aug
Sep
Oct
Nov
Dec
Month
10–15 km Partial Column O_3 Trends
b
O_3 Trend (%/decade)
25
20
15
10
5
0
−5
−10
−15
−20
−25
SC–Para
Nat–Asc
Nairobi
KL–Java
Samoa
Jan
Feb
Mar
Apr
May
Jun
Jul
Aug
Sep
Oct
Nov
Dec
Month

Figure 8.

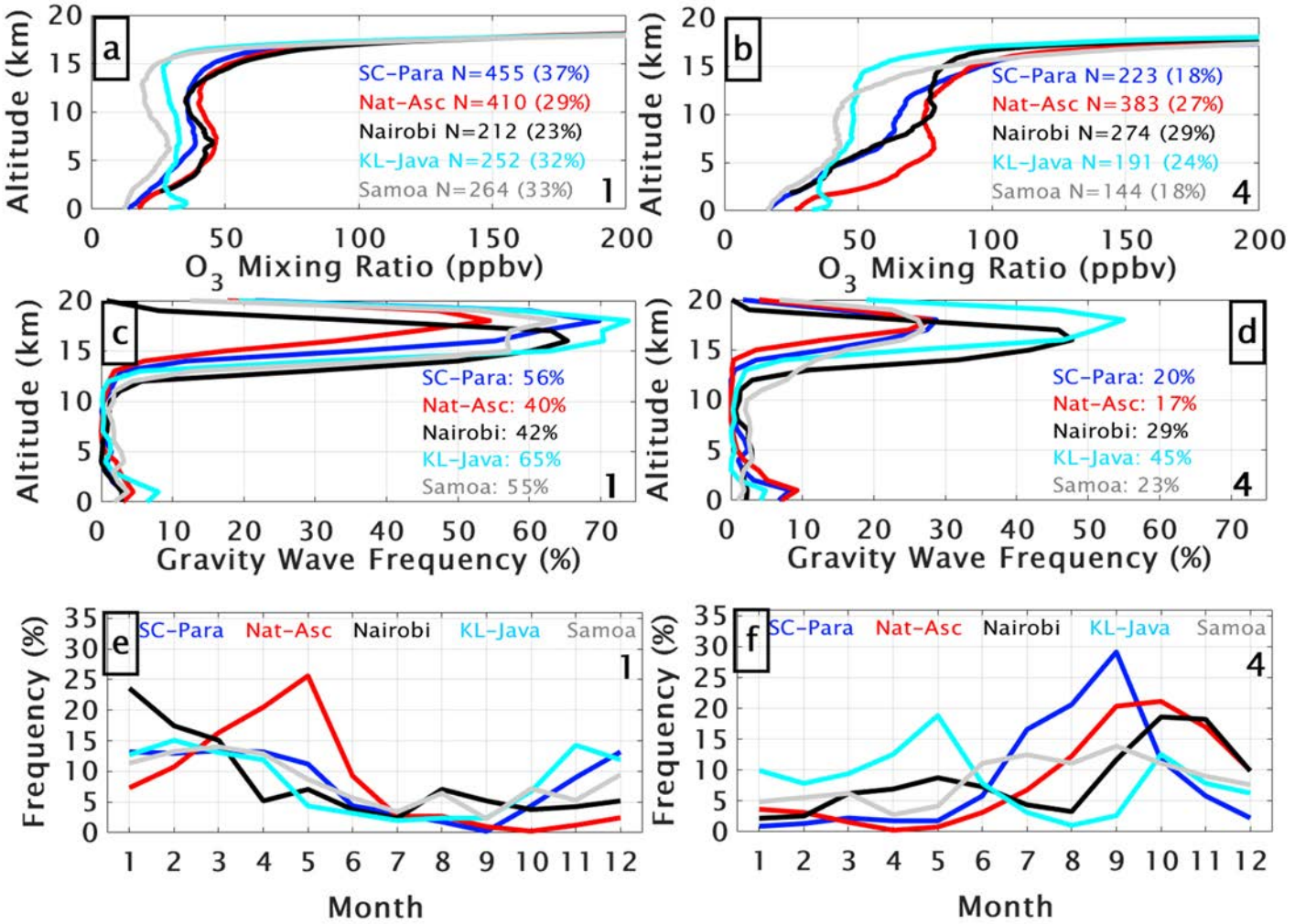
a
SC-Para N=455 (37%)
Nat-Asc N=410 (29%)
Nairobi N=212 (23%)
KL-Java N=252 (32%)
Samoa N=264 (33%)
1
Altitude (km)
O3 Mixing Ratio (ppbv)
b
SC-Para N=223 (18%)
Nat-Asc N=383 (27%)
Nairobi N=274 (29%)
KL-Java N=191 (24%)
Samoa N=144 (18%)
4
c
SC-Para: 56%
Nat-Asc: 40%
Nairobi: 42%
KL-Java: 65%
Samoa: 55%
Gravity Wave Frequency (%)
d
SC-Para: 20%
Nat-Asc: 17%
Nairobi: 29%
KL-Java: 45%
Samoa: 23%
e
SC-Para Nat-Asc Nairobi KL-Java Samoa
Frequency (%)
Month
f

Figure 9.

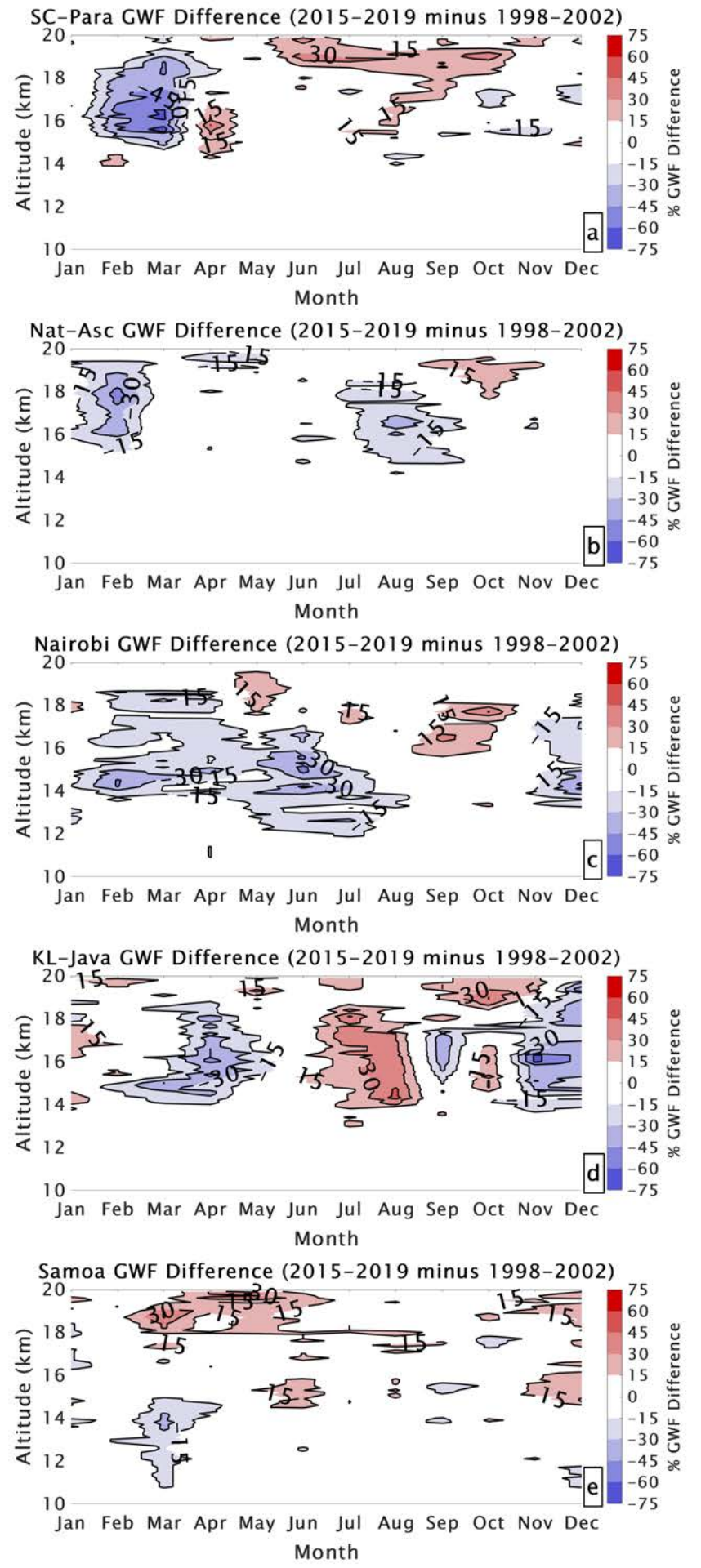
SC–Para GWF Difference (2015–2019 minus 1998–2002)
Nat–Asc GWF Difference (2015–2019 minus 1998–2002)
Nairobi GWF Difference (2015–2019 minus 1998–2002)
KL–Java GWF Difference (2015–2019 minus 1998–2002)
Samoa GWF Difference (2015–2019 minus 1998–2002)
Altitude (km)
Month
% GWF Difference
Jan Feb Mar Apr May Jun Jul Aug Sep Oct Nov Dec
a
b
c
d
e

Figure 10.

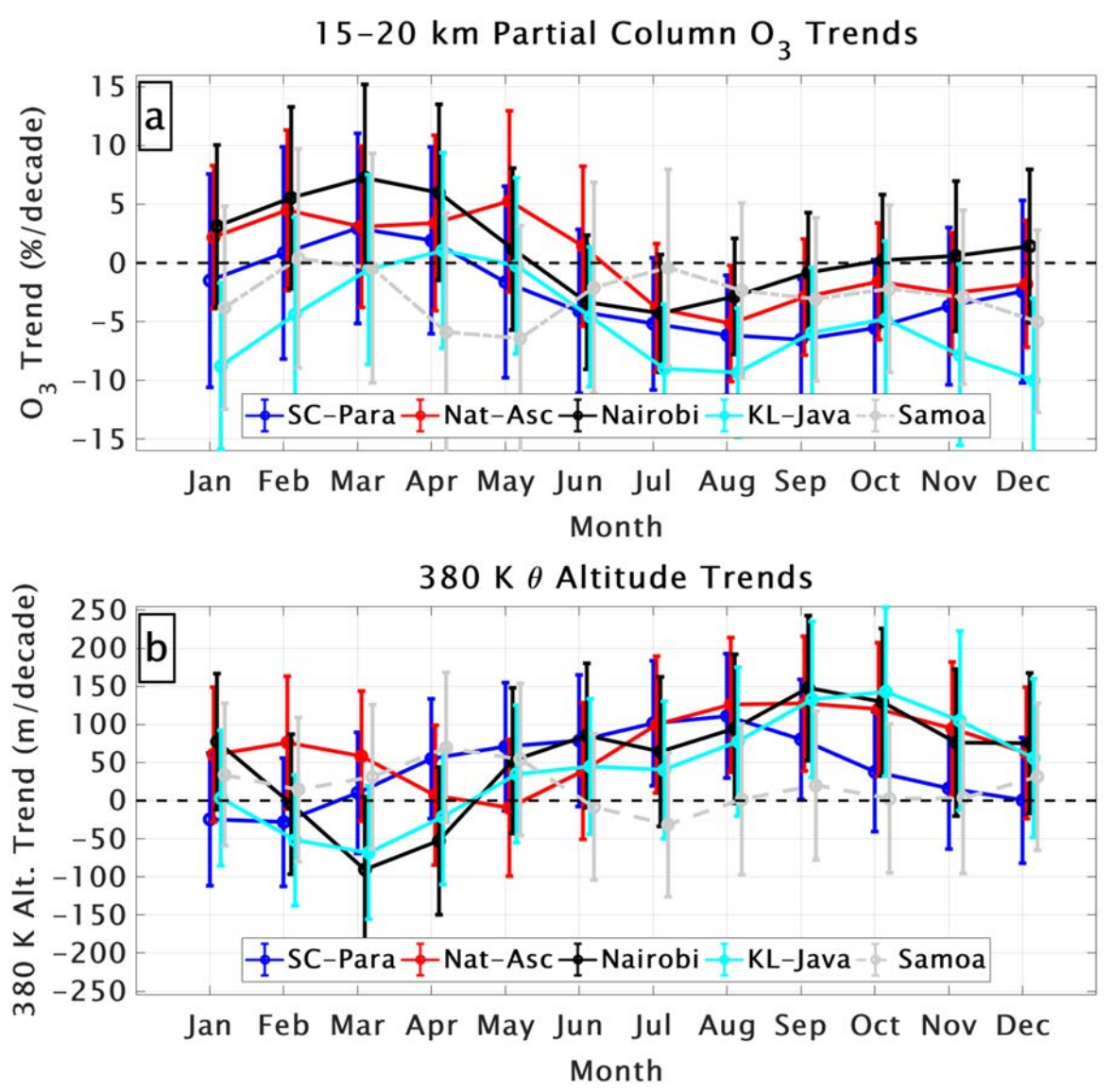
15–20 km Partial Column O_3 Trends
a
O_3 Trend (%/decade)
15
10
5
0
−5
−10
−15
SC–Para
Nat–Asc
Nairobi
KL–Java
Samoa
Jan Feb Mar Apr May Jun Jul Aug Sep Oct Nov Dec
Month
380 K θ Altitude Trends
b
380 K Alt. Trend (m/decade)
250
200
150
100
50
0
−50
−100
−150
−200
−250
SC–Para
Nat–Asc
Nairobi
KL–Java
Samoa
Jan Feb Mar Apr May Jun Jul Aug Sep Oct Nov Dec
Month

Figure 11.

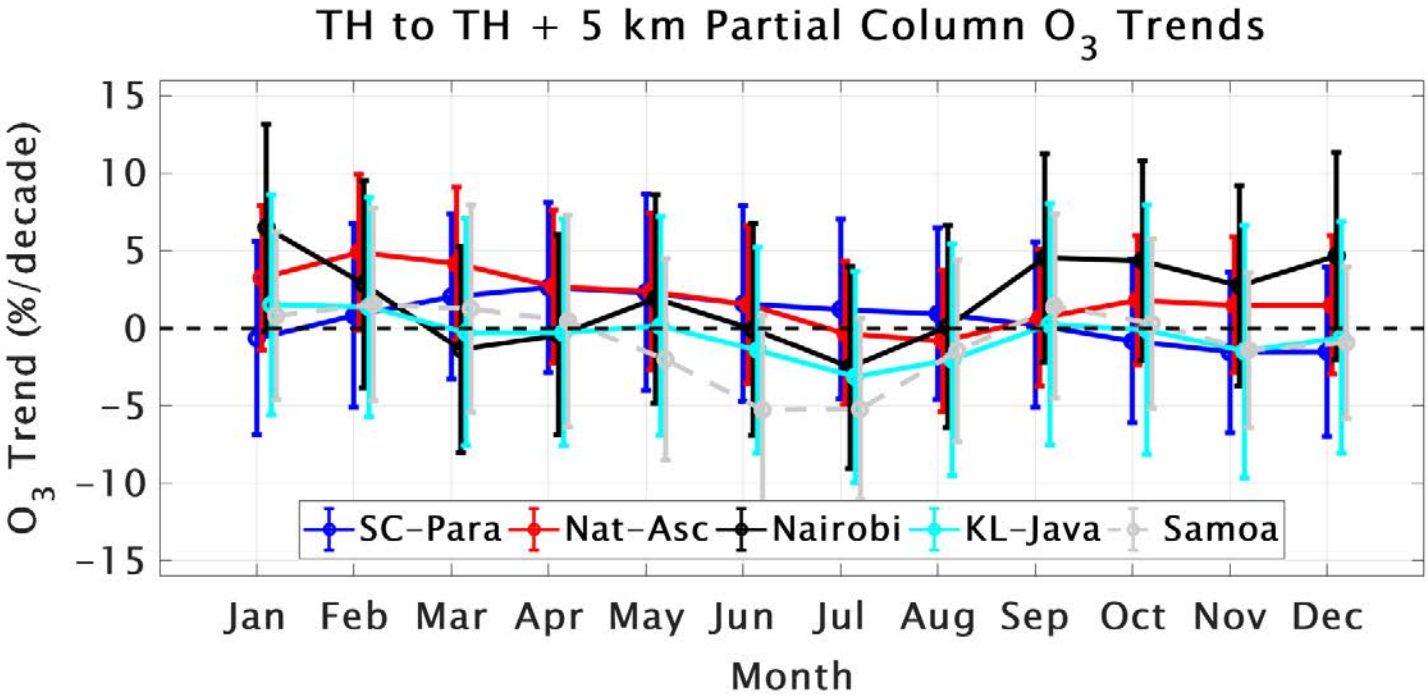
TH to TH + 5 km Partial Column O3 Trends
O3 Trend (%/decade)
15
10
5
0
−5
−10
−15
SC−Para
Nat−Asc
Nairobi
KL−Java
Samoa
Jan
Feb
Mar
Apr
May
Jun
Jul
Aug
Sep
Oct
Nov
Dec
Month

Journal of Geophysical Research Atmospheres

Supporting Information for

Regional and Seasonal Trends in Tropical Ozone from SHADOZ Profiles: Reference for Models and Satellite Products

Anne M. Thompson[1,2], Ryan M. Stauffer[1], Krzysztof Wargan[1,3], Jacquelyn C. Witte[4], Debra E. Kollonige[1,3], Jerald R. Ziemke[1,5]

[1]NASA/Goddard Space Flight Center (GSFC), Greenbelt, MD; [2]Joint Center for Environmental Systems Research, Univ of Maryland, Baltimore County, Baltimore, MD; [3]Science Systems and Applications, Inc., Lanham, MD; [4]National Center for Atmospheric Research Earth Observations Laboratory, Boulder, CO; Morgan State Univ., Baltimore, MD

Contents of this file

Figures S1 to S7; Tables T1, T2

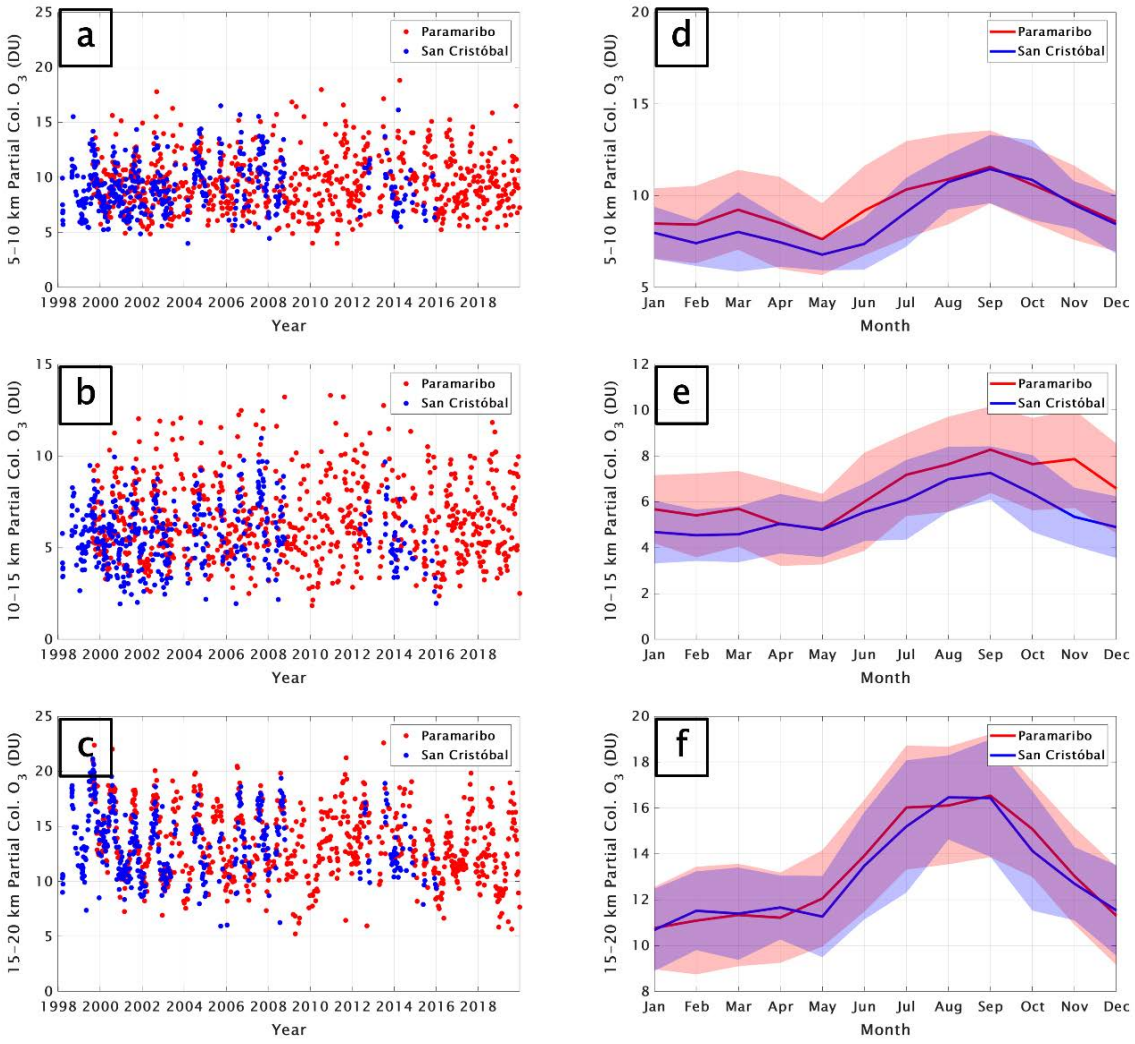

Figure S1. For the Paramaribo (red) and San Cristóbal (blue) SHADOZ data, the time-series (1998-2019) of ozone partial column amounts in (Dobson Units, DU) for (a) the lower FT, defined as 5-10 km; (b) upper FT, defined as 10-15 km; (c) LMS defined as 15-20 km. In (d-f): monthly mean partial column ozone (±1 σ) in DU based on the same soundings as for (a-c).

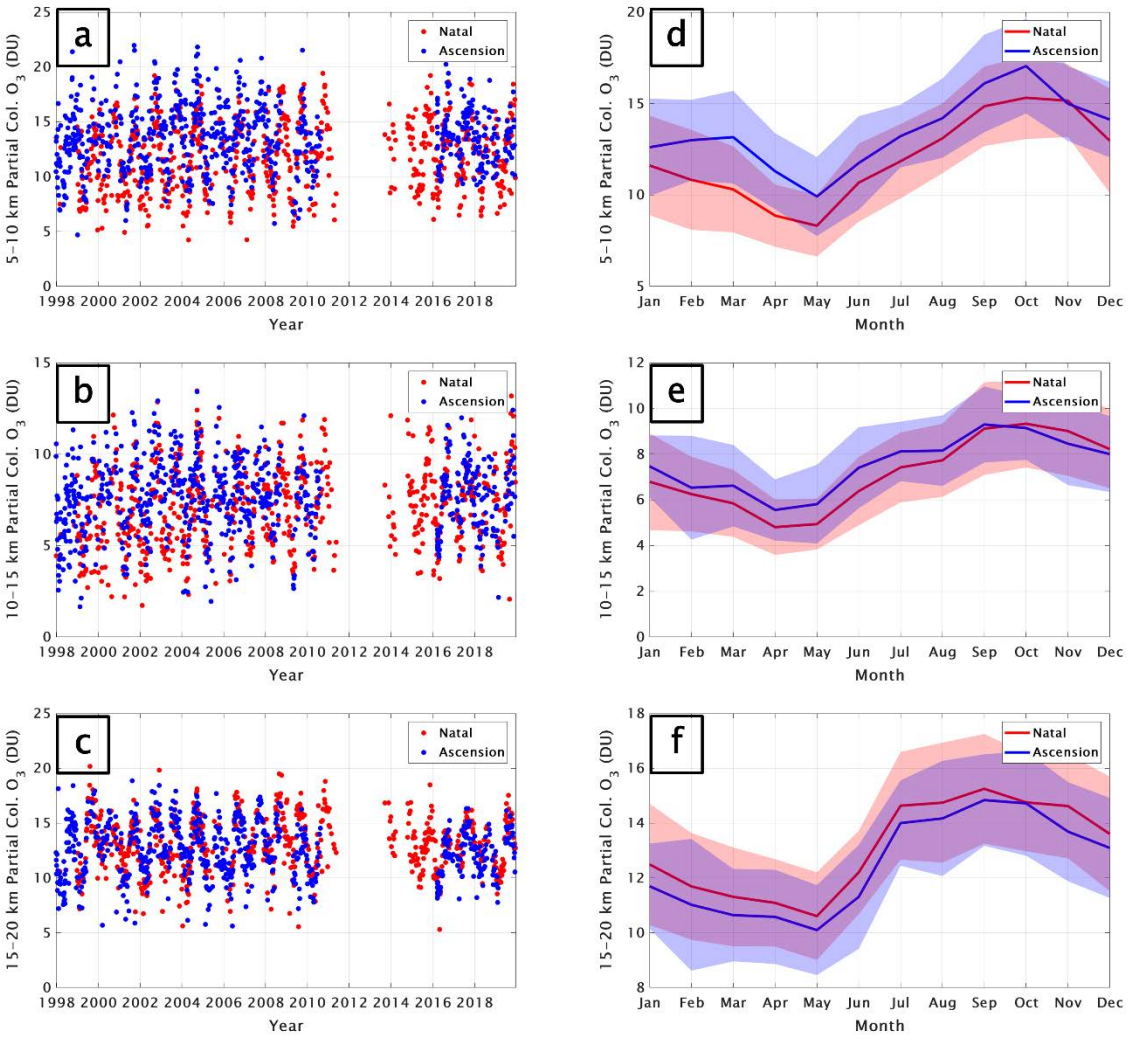

Figure S2. Same as for S1, except that the individual station data are from Natal (red) and Ascension (blue).

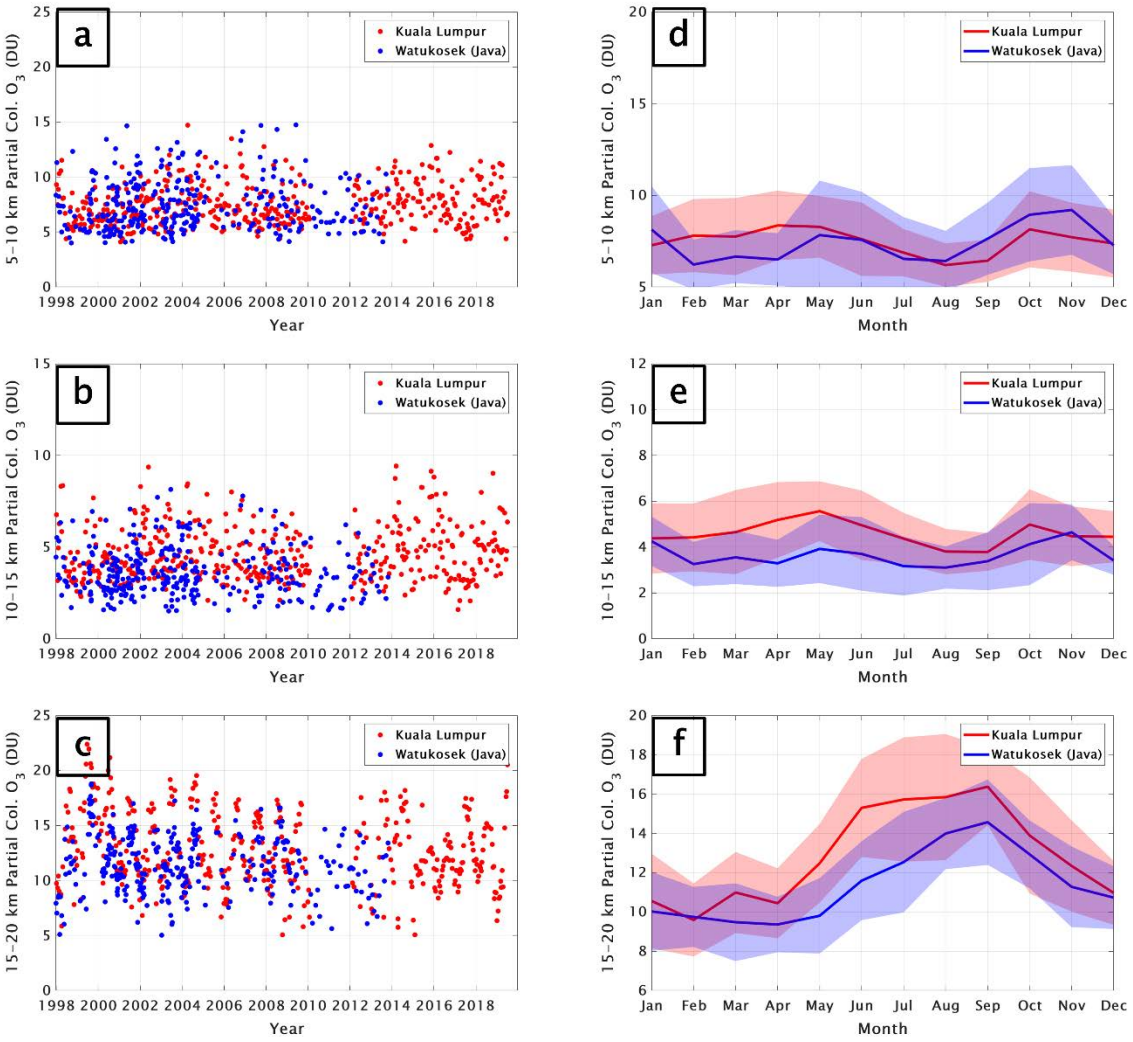

Figure S3. Same as for S1, except that the individual station data are from Kuala Lumpur (red) and Watukosek, Java, Indonesia (blue).

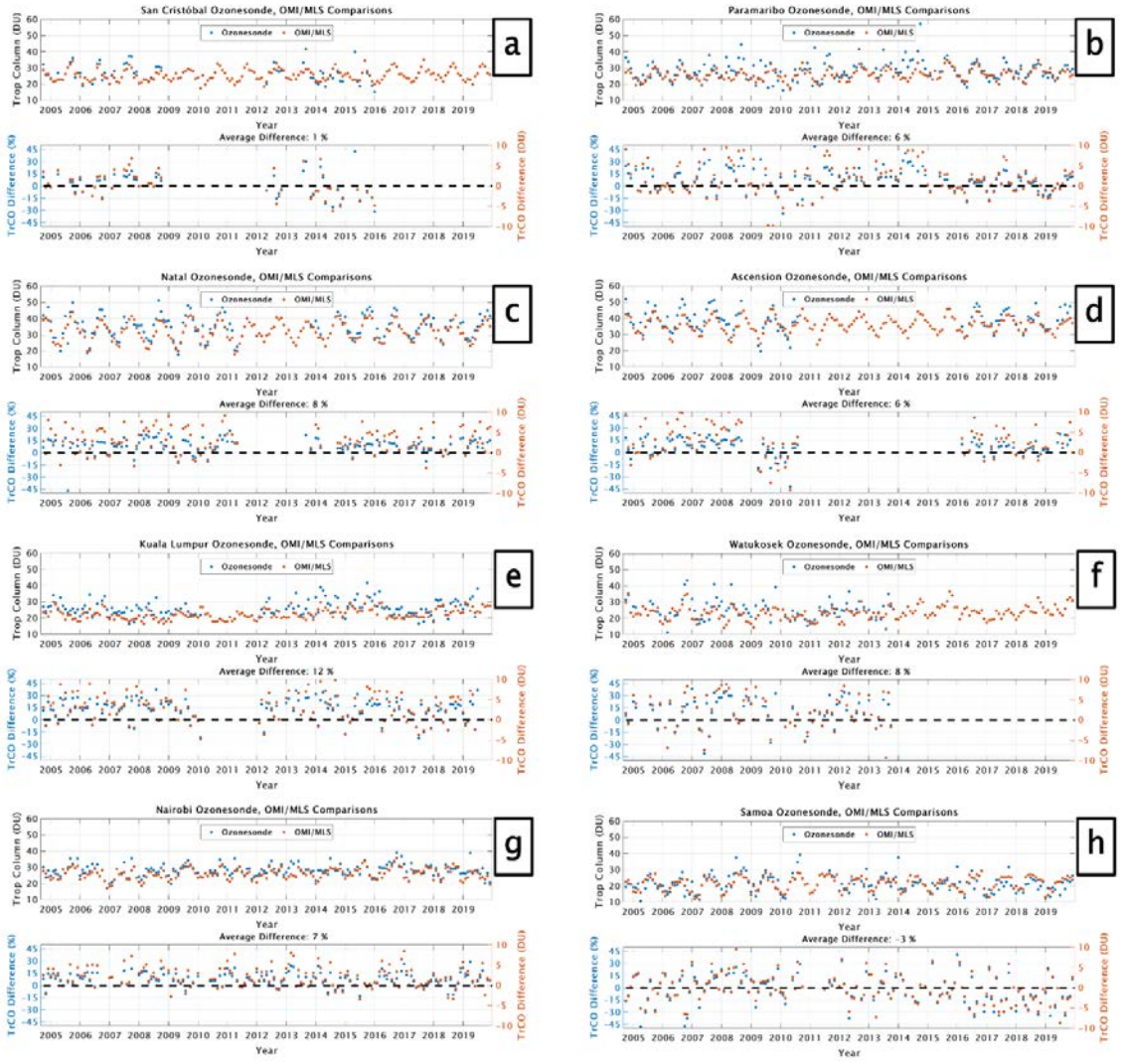

Figure S4. For the 8 stations analyzed, the upper panels in (a) –(h) give monthly mean tropospheric column ozone in DU, estimated from the OMI/MLS residual satellite product (*Ziemke et al.,* 2019) and integrated from surface to tropopause from SHADOZ data; the tropopause is determined from the radiosonde data. In text, the column integrals are referred to as $TrCO_{sat}$ for the OMI/MLS and $TrCO_{sonde}$ for the SHADOZ data. Lower panels give the difference between the two tropospheric columns in % (left scale, blue) and DU (right scale, red).

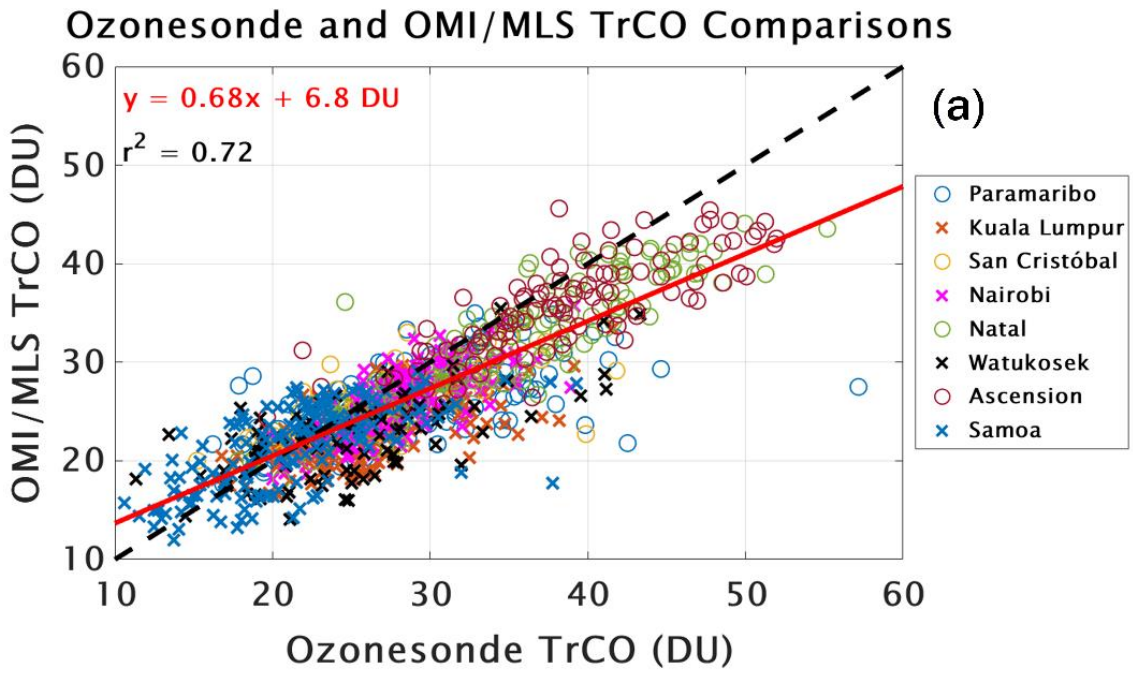

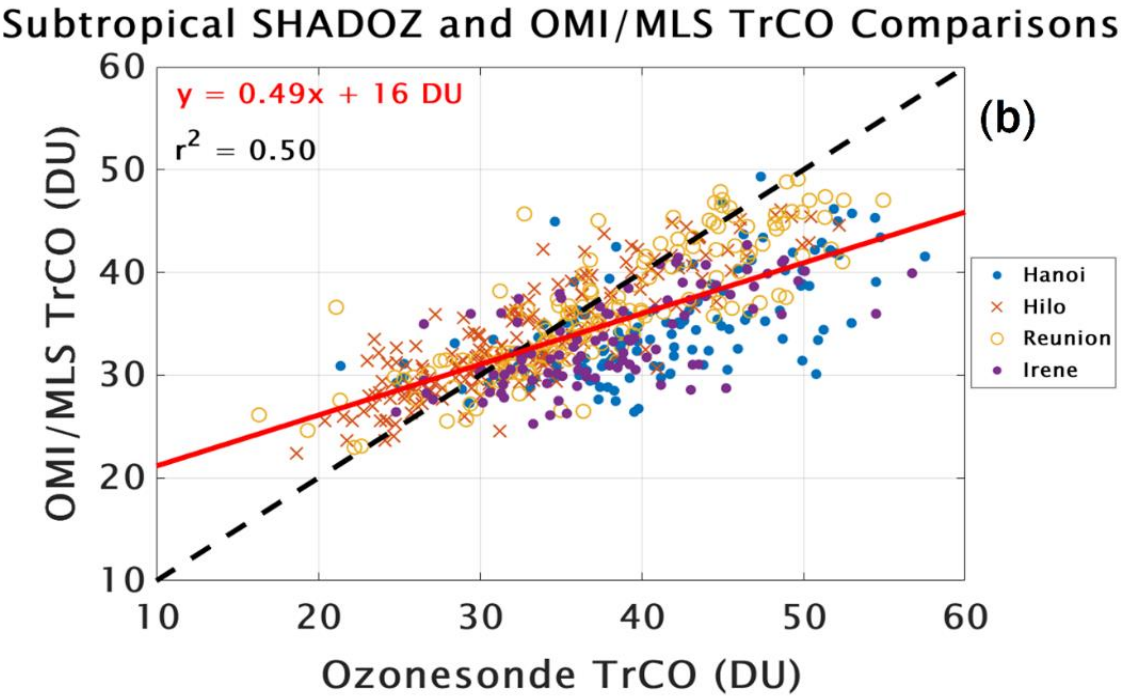

Figure S5. (a) Scatterplot of $TrCO_{sat}$ vs $TrCO_{sonde}$ for the 8 tropical SHADOZ stations in Figure S4; (b) same for the 4 subtropical SHADOZ stations, with latitude > 19N (Hilo, Hanoi) or > 19S (Réunion, Irene). The degraded correlation in the subtropics suggests caution in using OMI/MLS for determining tropospheric ozone trends at the higher latitudes.

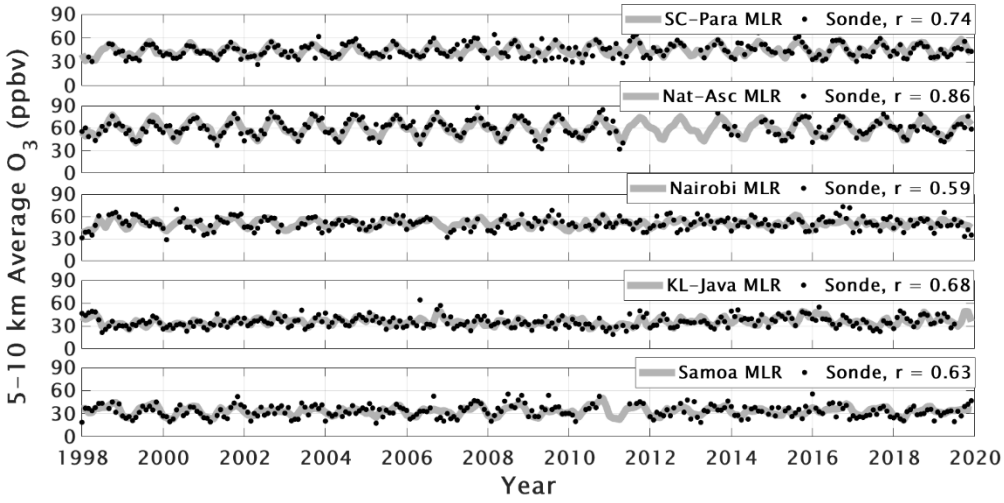

Figure S6. Monthly averaged MLR (grey lines) and ozonesonde (black dots) ozone mixing ratios for the two individual and three combination sites in the 5 to 10 km layer. Correlations between MLR model fits and ozonesonde data are shown in each frame.

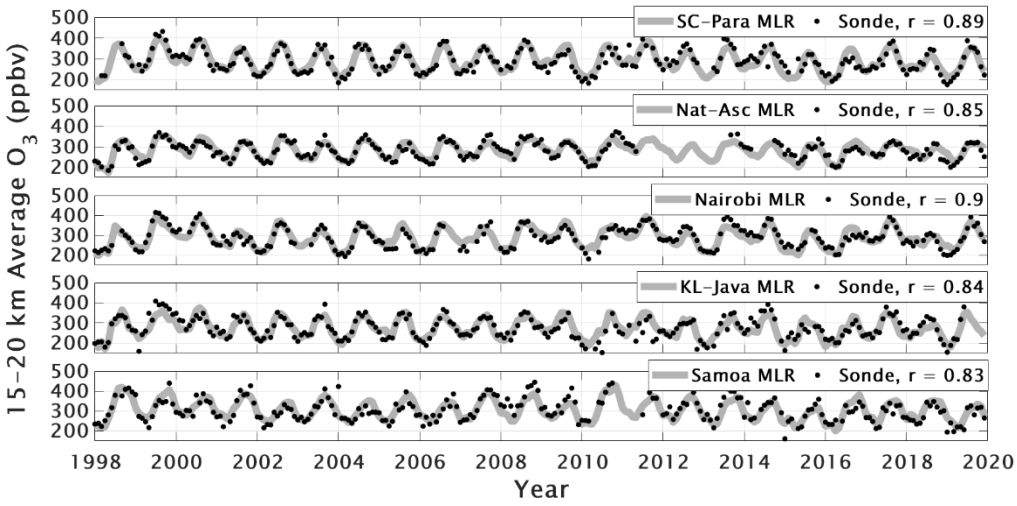

Figure S7. Monthly averaged MLR (grey lines) and ozonesonde (black dots) ozone mixing ratios for the two individual and three combination sites in the 15 to 20 km (LMS) layer. Correlations between MLR model fits and ozonesonde data are shown in each frame.

97

Table T1. Same as Table 1 except ozone change is in DU/decade

100

Trends by layer, DU per decade															
Site	**Lat, Lon (°)**	**Profiles**	**MLR Terms and Alt.**	**Jan**	**Feb**	**Mar**	**Apr**	**May**	**Jun**	**Jul**	**Aug**	**Sep**	**Oct**	**Nov**	**Dec**	**Ann**
SC+Para	-0.92, -89.62/5.8, -55.21	1227	MEI+QBO													
			5-10 km	-0.4±0.7 p = 0.233	0.1±0.7 p = 0.764	**0.7±0.7 p = 0.050**	0.5±0.6 p = 0.121	-0.0±0.7 p = 0.995	-0.1±0.7 p = 0.808	0.2±0.7 p = 0.609	0.3±0.7 p = 0.345	0.4±0.6 p = 0.271	0.4±0.6 p = 0.183	0.3±0.7 p = 0.435	-0.2±0.7 p = 0.470	0.2±0.3 p = 0.079
			10-15 km	-0.4±0.6 p = 0.162	-0.3±0.6 p = 0.336	0.2±0.5 p = 0.361	0.5±0.5 p = 0.055	0.2±0.6 p = 0.511	-0.2±0.6 p = 0.540	-0.0±0.6 p = 0.942	0.4±0.6 p = 0.155	0.5±0.5 p = 0.081	0.3±0.5 p = 0.343	0.0±0.5 p = 0.904	-0.2±0.6 p = 0.487	0.1±0.2 p = 0.260
			15-20 km	-0.2±1.0 p = 0.733	0.1±1.0 p = 0.848	0.3±0.9 p = 0.456	0.2±0.9 p = 0.623	-0.2±0.9 p = 0.688	-0.6±1.0 p = 0.231	-0.9±0.9 p = 0.070	**-1.1±0.9 p = 0.020**	**-1.1±0.9 p = 0.013**	-0.9±0.9 p = 0.060	-0.5±0.9 p = 0.265	-0.3±0.9 p = 0.517	**-0.4±0.4 p = 0.021**
Natal+Ascen	-5.42, -35.38/-7.58, -14.24	1436	MEI+QBO													
			5-10 km	0.3±0.7 p = 0.357	0.3±0.7 p = 0.445	0.3±0.7 p = 0.471	0.4±0.8 p = 0.283	0.6±0.7 p = 0.078	**0.8±0.7 p = 0.036**	0.6±0.7 p = 0.114	0.1±0.7 p = 0.850	-0.4±0.7 p = 0.253	-0.5±0.7 p = 0.196	-0.2±0.7 p = 0.668	0.2±0.7 p = 0.560	0.2±0.3 p = 0.143
			10-15 km	0.5±0.5 p = 0.059	**0.5±0.5 p = 0.042**	0.3±0.5 p = 0.198	0.1±0.5 p = 0.595	0.2±0.5 p = 0.423	0.4±0.5 p = 0.100	**0.5±0.5 p = 0.044**	0.4±0.5 p = 0.093	0.2±0.5 p = 0.411	0.0±0.5 p = 0.919	0.0±0.5 p = 0.894	0.2±0.5 p = 0.318	**0.3±0.2 p = 0.001**
			15-20 km	0.3±0.7 p = 0.454	0.5±0.7 p = 0.177	0.3±0.7 p = 0.341	0.3±0.8 p = 0.329	0.5±0.7 p = 0.159	0.2±0.8 p = 0.639	-0.6±0.8 p = 0.146	**-0.8±0.8 p = 0.040**	-0.4±0.8 p = 0.215	-0.2±0.8 p = 0.502	-0.4±0.8 p = 0.297	-0.2±0.7 p = 0.477	-0.0±0.3 p = 0.528
Nairobi	-1.27, 36.8	941	MEI+QBO													
			5-10 km	0.2±0.7 p = 0.639	**0.9±0.7 p = 0.018**	**1.2±0.8 p = 0.001**	0.6±0.8 p = 0.140	-0.4±0.8 p = 0.297	-0.6±0.8 p = 0.125	-0.2±0.8 p = 0.701	0.0±0.8 p = 0.997	-0.2±0.8 p = 0.679	-0.1±0.8 p = 0.769	0.0±0.8 p = 0.923	0.0±0.8 p = 0.991	0.1±0.3 p = 0.119
			10-15 km	0.0±0.6 p = 0.979	0.3±0.6 p = 0.350	0.6±0.6 p = 0.059	0.5±0.6 p = 0.093	0.1±0.6 p = 0.615	0.0±0.6 p = 0.989	0.1±0.6 p = 0.838	-0.1±0.6 p = 0.603	-0.6±0.6 p = 0.062	**-0.6±0.6 p = 0.035**	-0.3±0.6 p = 0.271	-0.1±0.6 p = 0.780	-0.0±0.2 p = 0.707
			15-20 km	0.3±0.8 p = 0.376	0.6±0.8 p = 0.152	0.7±0.8 p = 0.066	0.6±0.8 p = 0.110	0.1±0.8 p = 0.736	-0.5±0.8 p = 0.242	-0.7±0.8 p = 0.089	-0.5±0.8 p = 0.249	-0.1±0.8 p = 0.742	0.0±0.8 p = 0.940	0.1±0.8 p = 0.853	0.2±0.8 p = 0.670	0.1±0.3 p = 0.553
KL+Java	2.73, 101.27/-7.5, 112.6	786	MEI+QBO+IOD													
			5-10 km	-0.0±0.5 p = 0.947	**0.8±0.5 p = 0.001**	**0.9±0.5 p = 0.000**	0.3±0.5 p = 0.267	-0.2±0.5 p = 0.327	-0.2±0.5 p = 0.441	0.0±0.5 p = 0.991	0.1±0.5 p = 0.665	0.3±0.5 p = 0.317	0.3±0.6 p = 0.353	-0.1±0.7 p = 0.660	-0.5±0.6 p = 0.102	0.1±0.2 p = 0.138
			10-15 km	-0.1±0.3 p = 0.456	0.1±0.3 p = 0.466	**0.4±0.3 p = 0.005**	**0.5±0.3 p = 0.000**	0.2±0.3 p = 0.133	-0.2±0.3 p = 0.173	-0.3±0.3 p = 0.053	-0.1±0.3 p = 0.500	-0.1±0.3 p = 0.757	-0.2±0.4 p = 0.231	-0.3±0.4 p = 0.120	-0.3±0.4 p = 0.180	-0.0±0.1 p = 0.347
			15-20 km	**-1.0±0.8 p = 0.015**	-0.4±0.8 p = 0.289	-0.1±0.8 p = 0.898	0.1±0.8 p = 0.795	-0.0±0.8 p = 0.942	-0.6±0.8 p = 0.122	**-1.3±0.8 p = 0.001**	**-1.4±0.9 p = 0.001**	**-0.9±0.9 p = 0.035**	-0.7±0.9 p = 0.151	**-1.0±1.0 p = 0.043**	**-1.3±0.9 p = 0.005**	**-0.7±0.3 p = 0.000**
Samoa	-14.23, -170.56	795	MEI+QBO													
			5-10 km	0.5±0.8 p = 0.245	0.4±0.8 p = 0.322	0.3±0.8 p = 0.400	0.1±0.8 p = 0.770	-0.1±0.8 p = 0.822	-0.0±0.8 p = 0.912	0.0±0.8 p = 0.947	-0.2±0.9 p = 0.629	-0.4±0.8 p = 0.297	-0.2±0.8 p = 0.624	0.3±0.8 p = 0.460	0.5±0.8 p = 0.191	0.1±0.3 p = 0.226
			10-15 km	0.2±0.6 p = 0.448	0.4±0.6 p = 0.147	0.5±0.6 p = 0.123	0.3±0.6 p = 0.275	0.1±0.6 p = 0.780	-0.1±0.6 p = 0.720	-0.1±0.6 p = 0.779	0.1±0.6 p = 0.841	0.1±0.6 p = 0.808	-0.1±0.6 p = 0.778	-0.2±0.6 p = 0.562	-0.0±0.6 p = 0.878	0.1±0.3 p = 0.243
			15-20 km	-0.5±1.1 p = 0.377	0.0±1.1 p = 0.929	-0.1±1.1 p = 0.926	-0.7±1.2 p = 0.244	-0.8±1.2 p = 0.179	-0.3±1.2 p = 0.641	-0.1±1.2 p = 0.924	-0.4±1.2 p = 0.525	-0.5±1.2 p = 0.369	-0.4±1.2 p = 0.537	-0.5±1.2 p = 0.427	-0.7±1.2 p = 0.198	-0.4±0.5 p = 0.115

101
102

103

Table T2. Same as Table 2 except that ozone change is in DU/decade

106

Trends by layer, DU per decade															
Site	**Lat, Lon (°)**	**Profiles**	**MLR Terms and Alt.**	**Jan**	**Feb**	**Mar**	**Apr**	**May**	**Jun**	**Jul**	**Aug**	**Sep**	**Oct**	**Nov**	**Dec**	**Ann**
SC+Para	-0.92, -89.62/5.8, -55.21	1227	MEI+QBO													
			TH-10 to TH-5 km	-0.5±0.6 p = 0.076	-0.1±0.6 p = 0.624	0.4±0.6 p = 0.184	0.3±0.5 p = 0.242	-0.0±0.6 p = 0.939	-0.1±0.6 p = 0.841	0.1±0.6 p = 0.809	-0.0±0.6 p = 0.999	-0.1±0.5 p = 0.846	0.1±0.5 p = 0.626	0.1±0.6 p = 0.607	-0.3±0.6 p = 0.309	-0.0±0.2 p = 0.905
			TH-5 km to TH	-0.5±0.6 p = 0.127	-0.3±0.6 p = 0.373	0.2±0.5 p = 0.365	0.4±0.5 p = 0.134	0.1±0.6 p = 0.787	-0.1±0.6 p = 0.648	0.0±0.5 p = 0.878	0.2±0.5 p = 0.386	0.2±0.5 p = 0.505	0.1±0.5 p = 0.801	-0.0±0.5 p = 0.977	-0.2±0.5 p = 0.396	0.0±0.2 p = 0.875
			TH to TH+5 km	-0.2±1.7 p = 0.831	0.2±1.6 p = 0.783	0.6±1.5 p = 0.434	0.7±1.5 p = 0.328	0.6±1.7 p = 0.455	0.4±1.7 p = 0.608	0.3±1.6 p = 0.658	0.3±1.6 p = 0.728	0.1±1.5 p = 0.933	-0.2±1.5 p = 0.747	-0.5±1.5 p = 0.545	-0.4±1.6 p = 0.580	0.2±0.6 p = 0.428
Natal+Ascen	-5.42, -35.38/-7.58, -14.24	1436	MEI+QBO													
			TH-10 to TH-5 km	0.3±0.6 p = 0.239	0.3±0.6 p = 0.275	0.2±0.6 p = 0.542	0.3±0.6 p = 0.329	**0.7±0.6 p = 0.034**	**0.8±0.6 p = 0.013**	0.6±0.6 p = 0.064	0.1±0.6 p = 0.673	-0.2±0.6 p = 0.416	-0.4±0.6 p = 0.194	-0.3±0.6 p = 0.324	0.0±0.6 p = 0.878	0.2±0.3 p = 0.073
			TH-5 km to TH	**0.5±0.4 p = 0.021**	**0.6±0.4 p = 0.010**	0.3±0.4 p = 0.097	0.2±0.4 p = 0.363	0.3±0.4 p = 0.191	0.4±0.4 p = 0.066	0.4±0.4 p = 0.061	0.4±0.4 p = 0.074	0.3±0.4 p = 0.162	0.1±0.4 p = 0.572	0.0±0.4 p = 0.950	0.2±0.4 p = 0.333	**0.3±0.2 p = 0.000**
			TH to TH+5 km	0.8±1.1 p = 0.154	1.1±1.1 p = 0.051	0.9±1.1 p = 0.087	0.6±1.2 p = 0.270	0.5±1.2 p = 0.332	0.3±1.2 p = 0.535	-0.1±1.1 p = 0.892	-0.2±1.1 p = 0.713	0.2±1.1 p = 0.761	0.5±1.1 p = 0.380	0.4±1.1 p = 0.487	0.4±1.1 p = 0.501	0.5±0.5 p = 0.052
Nairobi	-1.27, 36.8	941	MEI+QBO													
			TH-10 to TH-5 km	-0.1±0.7 p = 0.719	0.3±0.7 p = 0.374	**0.8±0.7 p = 0.036**	0.5±0.8 p = 0.212	-0.3±0.8 p = 0.495	-0.5±0.7 p = 0.208	-0.2±0.8 p = 0.701	-0.0±0.8 p = 0.896	-0.2±0.7 p = 0.532	-0.2±0.8 p = 0.585	-0.0±0.8 p = 0.955	-0.1±0.7 p = 0.807	-0.0±0.3 p = 0.955
			TH-5 km to TH	0.0±0.5 p = 0.863	0.3±0.5 p = 0.214	**0.5±0.5 p = 0.042**	0.4±0.5 p = 0.125	0.1±0.5 p = 0.604	0.1±0.5 p = 0.651	0.2±0.5 p = 0.448	-0.0±0.5 p = 0.905	-0.4±0.5 p = 0.128	-0.4±0.5 p = 0.081	-0.2±0.5 p = 0.364	-0.1±0.5 p = 0.778	0.0±0.2 p = 0.205
			TH to TH+5 km	1.6±1.7 p = 0.056	0.7±1.7 p = 0.368	-0.4±1.7 p = 0.672	-0.1±1.7 p = 0.885	0.5±1.8 p = 0.550	-0.0±1.7 p = 0.980	-0.7±1.8 p = 0.421	0.0±1.8 p = 0.974	1.2±1.8 p = 0.172	1.2±1.8 p = 0.175	0.8±1.8 p = 0.378	1.2±1.7 p = 0.160	0.5±0.7 p = 0.079
KL+Java	2.73, 101.27/-7.5, 112.6	786	MEI+QBO+IOD													
			TH-10 to TH-5 km	-0.4±0.4 p = 0.092	0.3±0.4 p = 0.215	**0.7±0.4 p = 0.001**	**0.5±0.4 p = 0.015**	0.1±0.4 p = 0.813	-0.3±0.4 p = 0.153	-0.4±0.4 p = 0.082	-0.2±0.5 p = 0.318	0.0±0.5 p = 0.970	0.1±0.5 p = 0.813	-0.2±0.6 p = 0.420	**-0.5±0.5 p = 0.040**	-0.0±0.2 p = 0.306
			TH-5 km to TH	-0.1±0.3 p = 0.317	0.1±0.3 p = 0.418	0.2±0.3 p = 0.072	**0.5±0.3 p = 0.001**	**0.5±0.3 p = 0.003**	-0.1±0.3 p = 0.697	**-0.6±0.3 p = 0.000**	**-0.5±0.3 p = 0.003**	-0.2±0.3 p = 0.301	-0.2±0.3 p = 0.149	**-0.6±0.4 p = 0.004**	**-0.5±0.3 p = 0.004**	-0.1±0.1 p = 0.055
			TH to TH+5 km	0.4±1.9 p = 0.661	0.4±1.8 p = 0.684	-0.1±1.9 p = 0.940	-0.1±1.9 p = 0.934	0.0±1.9 p = 0.965	-0.4±1.9 p = 0.657	-0.9±1.9 p = 0.352	-0.5±2.0 p = 0.567	0.1±2.1 p = 0.947	-0.0±2.2 p = 0.981	-0.4±2.3 p = 0.703	-0.2±2.1 p = 0.868	-0.1±0.8 p = 0.621
Samoa	-14.23, -170.56	795	MEI+QBO													
			TH-10 to TH-5 km	0.6±0.7 p = 0.110	0.4±0.8 p = 0.320	0.2±0.8 p = 0.636	0.2±0.8 p = 0.696	0.1±0.8 p = 0.802	-0.0±0.8 p = 0.921	-0.1±0.8 p = 0.788	-0.1±0.8 p = 0.736	-0.2±0.8 p = 0.542	-0.3±0.8 p = 0.485	0.0±0.8 p = 0.921	0.5±0.8 p = 0.208	0.1±0.3 p = 0.270
			TH-5 km to TH	0.3±0.6 p = 0.345	0.3±0.6 p = 0.297	0.3±0.6 p = 0.424	0.1±0.7 p = 0.735	-0.1±0.7 p = 0.699	-0.3±0.7 p = 0.350	-0.2±0.7 p = 0.563	0.0±0.7 p = 0.902	0.0±0.7 p = 0.932	-0.2±0.7 p = 0.578	-0.2±0.7 p = 0.542	0.1±0.7 p = 0.861	0.0±0.3 p = 0.922
			TH to TH+5 km	0.2±1.6 p = 0.765	0.4±1.7 p = 0.620	0.3±1.7 p = 0.704	0.1±1.8 p = 0.896	-0.5±1.8 p = 0.544	-1.5±1.7 p = 0.083	-1.5±1.7 p = 0.073	-0.4±1.7 p = 0.622	0.4±1.7 p = 0.638	0.1±1.7 p = 0.911	-0.5±1.7 p = 0.574	-0.3±1.6 p = 0.711	-0.3±0.7 p = 0.310

107
108